Toward Controlled Fluidized Bed – Chemical Vapor Deposition of Boron Nitride: Thermochemical Analysis and Microstructural Investigations

Thomas Da Calva Mouillevois, Clément Rivière, Hervé Plaisantin, Jérôme Roger, Teresa Hungria, Georges Chollon, Nathalie Bertrand

Towards Controlled Fluidized Bed – Chemical Vapor Deposition of Boron Nitride: Thermochemical Analysis and Microstructural Investigations

CRediT authorship contribution statement

- 1st author: **Thomas DA CALVA MOUILLEVOIS**[1,2] *(corresponding author)*: dacalva@lcts.u-bordeaux.fr, Conceptualization, Methodology, Formal analysis, Investigation, Validation, Writing - Original Draft, Writing - Review & Editing, Visualization.
- 2nd author: **Clément RIVIÈRE**[2]: clement.riviere.1@outlook.com, Investigation.
- 3rd author: **Hervé PLAISANTIN**[1]: plaisantin@lcts.u-bordeaux.fr, Formal analysis, Investigation, Writing - Review & Editing.
- 4th author: **Jérôme ROGER**[1,2]: roger@lcts.u-bordeaux.fr, Formal analysis, Writing - Review & Editing.
- 5th author: **Teresa HUNGRIA**[3]: maria-teresa.hungria-hernandez@univ-tlse3.fr, Investigation, Writing - Review & Editing.
- 6th author: **Georges CHOLLON**[1]: chollon@lcts.u-bordeaux.fr, Conceptualization, Validation, Writing - Review & Editing, Supervision, Project administration.
- 7th author: **Nathalie BERTRAND**[1,2]: bertrand@lcts.u-bordeaux.fr, Conceptualization, Validation, Writing - Review & Editing, Supervision, Project administration.

[1] *ThermoStructural Composites Laboratory, CNRS – SAFRAN – CEA, 3 Allée de la Boétie, 33600 Pessac, France*

[2] *University of Bordeaux, 351 Cour de la Libération, 33400 Talence, France*

[3] *Raimond Castaing Microcharacterization Center, UT3, Toulouse INP, INSA Toulouse, CNRS, UT, 3 Rue Caroline Aigle, 31400 Toulouse, France*

Highlights

- Thermodynamic calculations and experimental studies of triethylamine borane precursor thermal decomposition.
- Optimization of the deposition parameters of stochiometric and free-carbon BN coating.
- Boron nitride coating in fluidized-bed CVD reactor on silicon carbide short fibers and powder.
- Fine physico-chemical and microstructural characterizations of boron nitride coating.
- Elaboration of boron nitride coating with low carbon and oxygen concentration.

Colors for figures

For a proper readability of the figures, all require color printing.

Abstract

This study examines the synthesis by fluidized bed chemical vapor deposition (FB-CVD), using triethylamine borane complex (TEAB) and the detailed characterization of stoichiometric and carbon-containing boron nitride (BN) interphases. The investigation highlights the importance of optimizing the CVD parameters to limit carbon contamination and explain the influence of carbon on the structure of the ex-TEAB deposit. The effects of deposition temperature, pressure, and dilution ratios of TEAB in ammonia and nitrogen (α and β), on the thermal decomposition of TEAB, as well as its impact on carbon contamination, are investigated through thermodynamic calculations. An infrared analysis experimentally confirms the great influence of TEAB dilution in ammonia (α) on the production of solid and gaseous phases. A high α ratio leads to a large production of hydrocyanic acid (HCN), which reduces carbon contamination and promotes the formation of stoichiometric BN. The evolution of the TEAB decomposition products, monitored by FTIR spectroscopy as a function of deposition parameters, is in good agreement with thermodynamic calculations. SEM characterizations of a low-carbon FB-CVD BN deposit reveal a dense, uniform in thickness, and adherent coating. TEM and EELS analyses conclude to a poorly crystalline and isotropic microstructure. AES and XPS confirm the presence of boron, nitrogen, and traces of carbon and oxygen. Carbon is not homogeneously distributed, but appears as a few disordered nano-sized inclusions in a more organized, pure BN continuum. Despite the use of a high-carbon precursor, nearly stoichiometric BN coatings were synthesized with low carbon and oxygen contamination, demonstrating the benefits of using non-chlorinated precursors.

Keywords

Chemical Vapor Deposition, Fluidized Bed, Boron nitride, Physico-chemical characterization, Coating

Table of contents

1. Introduction

Ceramic materials are stiff and usually exhibit a brittle behavior. However, some damage tolerance can be introduced into ceramic matrix composites (CMCs) by carefully controlling the interfaces/interphase between fibers and matrix [1]. This effect is characterized by a "pseudo-ductility", which is achieved by promoting crack deflection from the matrix (Mode I) to the fiber/matrix interface (Mode II). As a result, the composite is able to endure deformation without catastrophic failure. This is accomplished by introducing a preferential, or sacrificial, damage zone in the form of a thin layer between the fibers and matrix, otherwise referred to as "interphase". This interphase needs to be thermochemically compatible with the constituents of the CMC, exhibit strong adhesion, and withstand high operating temperatures. Additionally, the interphase must be weaker than the matrix to serve as a "mechanical fuse" [2]. If the interphase is too strong, it will increase the CMC's stiffness and brittleness, while a too weak interphase will result in premature damage and decrease load-carrying capacity. Therefore, to achieve pseudo-ductile behavior in the final material without limiting the maximum stresses, the interphase must maintain a balanced bond that is neither too strong nor too weak [3]. The commonly used interphase materials possess a layered crystalline structure, the layers being roughly parallel to the fiber surface and weakly bonded to each other, facilitating crack deflection and energy dissipation. Examples of such materials include pyrolytic carbon (PyC) and hexagonal boron nitride (h-BN).

Historically, the interphase used in CMCs was composed of PyC prepared by chemical vapor deposition or chemical vapor infiltration (CVD/CVI). Pyrolysis of various hydrocarbon precursors, such as methane [4–6], propane [1,7,8], propylene [9–11], ethylene [12–14], has been extensively studied. The selection of hydrocarbons as precursors has been motivated by their accessibility and affordability. Furthermore, in the gaseous state and under standard temperature and pressure conditions, their handling and transport to the reaction zone do not cause significant technological challenges. Ethanol and other bio-based precursors can also be considered [15–18].

Hexagonal boron nitride (h-BN) displays a combination of chemical, electrical, mechanical and thermal properties that make it well suited for a wide range of high-value industrial applications. Recently, hexagonal or turbostratic BN emerged as an interesting candidate for interphase coatings in CMCs, challenging the historically favored PyC interphase. Both graphite and boron nitride have hexagonal crystallographic structures with strong covalent bonding in the plane and weak bonding between planes. Although PyC and BN interphases are not strictly hexagonal but turbostratic. When exposed to standard CVD conditions, the dominant forms of boron nitride and carbon are inherently turbostratic, which implies the occurrence of stacking faults within the (002) planes. h-BN exhibits superior oxidation resistance compared to PyC due to its higher onset temperature of oxidation (800°C for h-BN compared to 400°C for PyC) [19]. However, turbostratic BN competes significantly with PyC only when the latter exhibits sufficient anisotropy. Indeed, anisotropic BN shows a better oxidation resistance than isotropic BN [20,21].

In the development of BN interphases, the most common precursors have been boron trichloride (BCl_3) [22–25] or boron trifluoride (BF_3) [26–28] as sources of boron, along with ammonia (NH_3) for nitrogen. Although these precursors were the subject of extensive study and yielded acceptable deposition, the major decomposition by-products, *i.e.*, HCl and HF, have caused significant damage to silicon carbide (SiC) fibers and chemical vapor deposition equipment, thus posing risks to experimenters. An alternative approach involves the use of organoboron precursors such as tris(dimethylamino) borane (TDMAB): $B(N(CH_3)_2)_3$ or triethylamine borane complex (TEAB): $(C_2H_5)_3N{\cdot}BH_3$. These single-source precursors are liquids at room temperature and contain both boron and nitrogen within the same molecule. Their initial B:C:N ratios are 1:6:3 and 1:6:1, respectively. Moreover, they offer several advantageous properties, including non-toxicity, non-explosiveness, room temperature stability, relatively high vapor pressures, and corrosive compatibility with fibers or CVD reactor-sensitive components. Due to the significant cost difference between the two precursors (around 2000 €.mol^{-1} for TDMAB and about 250 €.mol^{-1} for TEAB), the TEAB/NH_3/N_2 system was chosen for this study.

CMCs have primarily been developed using long woven fibers as continuous reinforcements. However, for certain applications, CMCs with discontinuous reinforcements could be advantageous. Discontinuous reinforcements, such as short fibers, facilitate processing and provide greater design flexibility for components having complex shapes, smaller thicknesses or properties requiring more isotropy. The FB-CVD process is particularly suitable to coat discontinuous reinforcements such as short fibers, and is well adapted to the use of novel liquid precursors such as TEAB. Nevertheless, adding the fluidization process to the CVD process itself introduces certain trade-offs. Although both operations need to work in tandem during deposition, their respective operating parameters would often need to be adjusted in opposite directions. For example, the gas flow rate is a crucial parameter for both charge fluidization and for CVD deposition. This parameter impacts the quality of gas-solid exchange, regulates fluidization regimes, and induces charge mixing, while the gas flow rate governs the entrainment of gas, varies precursor residence time in the reaction zone and affects the kinetic regime. The total flow rate is bounded at a low level by the minimum fluidization velocity (U_{mf}) and at a high level by the terminal free fall velocity of the particles (U_t). These constraints impact both the total flow rate and the precursor residence time in the hot zone. Generally, fluidization relies on velocities around multiple U_{mf}, resulting in residence times of some seconds. As a result, compromises must be made between fluidization and CVD deposition requirements.

Previous studies [18,29] have shown the ability to fluidize short fiber and powder mixtures at various proportions, temperatures and pressures. The temperature-related results have minimal effects on fluidization, and studies suggest that an optimal fluidization pressure of about 200 mbar. This pressure can be increased, *e.g.* to meet the requirements of CVD deposition, but it should not drop below 100 mbar due to the rarefied flows that significantly affect fluidization quality. Additionally, preliminary experiments have demonstrated the capability to not only fluidize mixtures of powders and short fibers, but also to predict the minimum fluidization velocity of such mixtures based on simplified parameters. These results have been put to use in the present study to meet the demands of interphase coating.

The objective of this study is to develop an interphase coating of stoichiometric BN using a new precursor (TEAB) on particulate mixtures and to characterize the chemical and structural properties of such coating in order to evaluate its potential application as an interphase in CMCs. To achieve this, we perform thermodynamic calculations of the TEAB/NH_3/N_2 system to predict the optimal deposition conditions for the boron nitride interphase as a function of the deposition temperature, initial dilution ratios ($\alpha = {Q_{NH_3}}/{Q_{TEAB}}$ and $\beta = {Q_{N_2}}/{Q_{TEAB} + Q_{NH_3}}$) and total pressure. The thermodynamic calculations are then compared with the experimental results of a Fourier Transform Infrared (FTIR) spectroscopy study of the decomposition of TEAB. These preliminary investigations provide guidance for the selection of CVD parameters. The coatings are finally thoroughly characterized using Scanning Electron Microscopy (SEM), Transmission Electron Microscopy (TEM), Electron Energy Loss Spectroscopy (EELS), Auger Electron Spectroscopy (AES) and X-ray Photoelectron Spectroscopy (XPS).

2. Materials and methods

2.1. Synthesis

The coatings are synthesized with a fluidized bed reactor. Further description of the reactor can be found in [18]. To protect the reactor's sensitive components from overheating, the column is initially filled with 580 g of zirconia beads with a diameter of 0.5 mm [30], to raise the particle bed to the heating elements level. A mixture of SIKA® TECH SiC powders (from Fiven) and desized SiC Hi-Nicalon type S short fibers (from NGS Advanced Fibers Co., Ltd) is added into the fluidization column. The mixture is mixed and maintained in the fluidized bed for several minutes at a high nitrogen flow rate exceeding 2000 sccm. The column is then placed under vacuum for several hours before the pressure being raised to 200 mbar for the coating. The precursor (TEAB) is then fed under pressure into a commercial evaporator (from 2M Process). The evaporator combines the liquid precursor with nitrogen in aerosol form. The volumetric flow rate of TEAB is measured and controlled by a Coriolis flowmeter. The aerosol is heated inside the evaporator cell and transported to the bottom of the column via an insulated line. The ammonia conveying line is also heated to prevent cold spots and recondensation of the liquid precursor during the precursor mixture before it reaches the reaction zone. The heating elements are gradually warmed to the coating temperature and then stabilized before the injection of the precursors. At the outlet, precursor decomposition by-products are trapped by a series of cold traps and particle filters to prevent fine particles from entering the pumping system. Following the coating process, the particle bed is recovered, sieved, and analyzed using the various characterization methods described below. Prior to its injection in gaseous form, when liquid TEAB is heated to its evaporation temperature, it may gradually gel, leading to clogging of the small section pipes (1/8”). To prevent interruptions to the deposition process, and considering the relatively low deposition rates (a few tens of nanometers per hour only), it was chosen to purge the whole injection system at least every two hours. In the present case, the coating is deposited in four steps, *i.e.* 1h + 2h + 1h + 2h, for a cumulative deposition duration of 6h.

2.2. Thermodynamic calculations

Preliminary thermodynamic analyses of the equilibrium starting from the TEAB/NH_3/N_2 system are performed using Thermo-Calc [31]. The thermodynamic equilibrium is calculated based on the CALPHAD (CALculation of PHAse Diagrams) methodology [32,33]. The thermodynamic assessments of the solids and the gaseous species were obtained from the NIST Chemistry WebBook [34], the NASA database [35] and the B-C system [36]. Calculations take into account atomic ratios B ; C ; N and H, as a function of dilutions ratios $\alpha = {Q_{NH_3}}/{Q_{TEAB}}$ and $\beta = {Q_{N_2}}/{Q_{TEAB} + Q_{NH_3}}$ (with Q_X the volumetric flow of the X gas) equal to $\frac{1}{\Sigma}$; $\frac{6}{\Sigma}$; $\frac{1+\alpha+2\beta(1+\alpha)}{\Sigma}$ and $\frac{18+3\alpha}{\Sigma}$ respectively, with $\Sigma = 26 + 4\alpha + 2\beta(1+\alpha)$ and constant total pressure. The mole fractions are plotted versus temperature with and interval of 10°C. The range of the parameters used here is considered within the limitations of the CVD reactor installation, except for the temperature, which is extended to 1100°C. Only one parameter is varied while the others are held constant. Optimization by parameter combinations was not performed here, the thermodynamic calculations are mainly aimed at identifying the most influential CVD parameters. For clarity, only species with a mole fraction higher than 10^{-6} are shown here.

2.3. Characterizations techniques

Since no morphological or compositional disparities were observed between the fiber and powder deposits, the physico-chemical characterizations were conducted on the fibers. Their regular cylindrical geometry indeed facilitates the identification of the orientation of the deposit axis relative to the substrate.

2.3.1. SEM/EDX analysis

The coatings are examined by Scanning Electron Microscopy (SEM), utilizing either a SEM FEI Quanta 400 FEG V3® or a Hitachi S4500 FEG. Microscopic images are captured with an acceleration voltage set at 5 kV (FEI Quanta) or 3 kV (Hitachi), for optimal resolution and minimal interaction disturbance. X-ray Energy Dispersive Spectroscopy (EDS) analysis are performed with a FEI Quanta SEM equipped with a 100 mm^2 EDS Ultim Premium detector, operating at a minimal 5 keV acceleration voltage for surface analysis of thin coatings (< 100 nm). Prior to the EDS-SEM analysis of deposits, the particles underwent a special procedure were the coated particles are cold pressed with copper powder, embedded in epoxy resin and cut to get cross-sectional views of the coatings.

2.3.2. Auger analysis

The Auger Electron Spectroscopy (AES) analysis was conducted using an ULVAC-Phi AUGER PHI 710 nanosonde with an Ar^+ ion gun to produce depth profiles. The probe had a diameter of 10 nm and an interaction depth of 5 nm. To prevent charge artifacts, sample inclination was applied. The AES was stimulated by incident electrons (5-25 keV). The emitted electron spectra (50 eV to 2.5 keV) were recorded for elemental identification and elemental quantification. The concentration precision achieved was $5\%_{at.}$.

2.3.3. XPS analysis

A ThermoFisher Scientific K-ALPHA spectrometer was used for X-ray Photoelectron Spectroscopy (XPS) surface analysis with a monochromated Al-Kα source ($h\nu = 1486.6$ eV) and a 200 µm X-ray spot size. The powders were pressed onto indium foils, and the entire spectra (0-800 eV) were acquired using a constant pass energy of 200 eV, while high-resolution spectra were captured with a constant pass energy of 40 eV. Charge neutralization was applied during the analysis, and depth profiles were acquired using an Ar+ ion gun, with 360s sputtering between each level. High-resolution spectra (C_{1s}, O_{1s}, Si_{2p}, N_{1s}, B_{1s}) were measured using the Avantage software provided by ThermoFisher Scientific, employing Scofield sensitivity factors. Before sputtering, the XPS spectra were initially recorded to prevent alterations in the binding energies. Slight Ar^+ sputtering was performed to eliminate surface contamination and verify the elemental composition's uniformity through depth. The binding energy values used to fit the spectra and the corresponding atomic environments are summarized in Table 1.

Table 1 : Chemical compounds, atomic environments and related binding energies used for the fitting of the B_{1s}, N_{1s} and C_{1s} XPS spectra [37].

	B_{1s}	
B_2O_3	B-O_3	192.8 eV
"Oxydes"	B-C_nO_{3-n}/B-N_nO_{3-n}	191.8 eV
h-BN	B-N_3	190.7 eV
h-B-C-N	B-N_nC_{3-n}	189.5 eV
h-B-C	B-B_nC_{3-n}	188.4 eV
B_4C/h-B-C	-/B-C_3	187.5 eV
B (clusters)	-	186.6 eV
	N_{1s}	
"Oxydes"	N-C_nO_{3-n}	400.8 eV
h-B-C-N/oxidized h-BN	N-C_3/N-O_nB_{3-n}	399.9 eV
h-B-C-N	N-C_nB_{3-n}	398.7 eV
h-BN	N-B_3	397.4 eV
	C_{1s}	
h-B-C-N	C-N_nB_{3-n}	285.8 eV
h-B-C-N/C sp^3	C-N_nB_{3-n}/-	285.0 eV
h-C (sp^2, graphite)	C-C_3	284.3 eV
Oxidized carbide	C-B_nC_{3-n}/C-B_nO_{3-n}	283.6 eV
h-B-C/carbide (SiC)	C-B_nC_{3-n}/C-Si_4	282.6 eV
B_4C	C-B_4	281.7 eV

2.3.4. TEM and EELS analysis

For Transmission Electron Microscopy (TEM) analysis, samples of coated particles were embedded in epoxy resin, cut with a wire saw, and mechanically thinned to a thickness of approximately 100 µm. These thin cross sections containing coated fibers were then processed using Ar^+ ion beam milling

(JEOL, IonSlicer, EM-09100IS) until electron transparency was achieved. The study employed conventional Transmission Electron Microscopy (TEM) to analyze samples using Bright Field (BF), Dark Field (DF), and High Resolution (HR) modes. A CM30ST microscope (Philips, Thermofischer) was used, operating at 300 kV with a LaB_6 source. The DF images were generated via electron beam scattering from sp^2-BN basal atomic layers spaced between 0.3 and 0.4 nm. HR-TEM images were obtained from the thinnest parts of the thin foils. SAD patterns were acquired from areas of 400 nm in diameter to determine the microstructural organization of turbostratic BN using two parameters derived from the SAD patterns. The first parameter quantify the structural anisotropy, using the method employed by Bourrat *et al.* for pyrocarbon [38]. The experiment involved measuring the orientation angle (OA), *i.e.* the azimuthal opening of the arc related to the first-order reflection of the sp^2-hybridized atom basal layers. If the intensity remains constant along the radius circle of 0.3-0.4 nm, the material is therefore assumed to be isotropic. The second parameter is the coherence length L_c and is measured from the full width at half maximum of the radial intensity of the arcs using a Scherrer-type equation, as in X-ray diffraction analysis [39]. The (OA, L_c) values for a given coating were averaged from 3 SAD patterns obtained from various fiber coatings. Additional imaging techniques including Scanning Transmission Electron Microscopy in High Angular Annular Dark-Field mode (STEM-HAADF), and Electron Energy Loss Spectroscopy (EELS) analysis were carried out at the "Centre de microcaractérisation Raimond Castaing" (UAR 3623) in Toulouse, France. A JEOL JEM-ARM200F microscope equipped with a cold FEG source operating at 200 kV was used. STEM-HAADF imagery was carried out with a GATAN and a JEOL detector, and EELS spectrometry with the GATAN GIF QUANTUM ER, using two different dispersions values 0.1 eV/channel and 0.25 eV/channel, with a resolution of 0.6 eV and 1 eV, respectively.

2.3.5. FTIR analysis

The Fourier Transform Infrared (FTIR) spectra were recorded from the gas phase after thermal decomposition of the precursors in a second convenional vertical reactor, which is also used for CVD coating on static substrates [40]. The reactor is equipped with a 700 mm long silica tube having an internal diameter of 35 mm. Heating is accomplished through a radio-frequency induction system placed outside the tube, and the reactor walls are coated with expanded graphite. The pressure in the reactor is regulated by a motorized valve and a pressure sensor. Gases are transported from the top of the reactor, passing through the hot deposition zone, the gas cell at the exit (at room temperature for the infrared analysis) and eventually in two cryogenic traps prior to arriving at the vacuum pump. The gas analysis cell is equipped with two ZnSe portholes at both ends. The infrared spectra are acquired using an MCT-A detector in ex-situ configuration. The reactor's temperature is regulated with a Eurotherm controller, which is connected to a CELES inductive heating generator. The temperature is raised at a rate of 30°C per minute and stabilized several minutes to stabilize the hot gas temperature and eliminate any impurities. Once the infrared signal is free of any contaminant, a blank spectrum is recorded and the precursors are injected through a bubbler. The mixture of TEAB and N_2 is then carried to the reactor in pure heated nitrogen, flowing through the bubbler heated in a water bath. The reactor undergoes cleaning by heating up to 900°C under a pure nitrogen flow for a few hours between each FTIR acquisition. Spectra are acquired with Thermo Fisher Scientific's OMNIC software and processed using TQAnalyst software.

3. Results and discussion

3.1. BN coating

Control of the BN coating process is essentially governed by the parameters of the CVD process. These essential parameters include: the initial dilution ratio between ammonia and TEAB flow rates ($\alpha = {Q_{NH_3}}/{Q_{TEAB}}$), the initial dilution ratio between nitrogen and precursor flow rates ($\beta = {Q_{N_2}}/{Q_{TEAB} + Q_{NH_3}}$), the total flow rate ($Q_{tot}$), the deposition temperature (T) and the total reactor pressure (P).

Experimental, thermodynamic, and literature data all support the need to add ammonia in excess to get pure BN [41–43]. Some authors even recommend an α ratio such as $\alpha > 10$ [44]. Indeed, a high α ratio decreases the amount of carbon in coatings [45,46] and reduces the operating temperature [44]. The effect of the initial partial pressure and of the total total flow rate are not clearly analyzed in the literature. The growth rate was founded to increase linearly with the square root of the precursor flow rate [44]. Numerous studies have investigated the role of the coating temperature, commonly ranging from 600 to 900°C. TEAB decomposes when exposed to temperatures exceeding 500°C and, above a certain temperature (~ 850°C with NH_3 added), the breaking of amine bonds leads to an increase of the carbon concentration in the coating [45]. The literature consistently reports the coating of h-BN from TEAB under low reactor pressures, below 1 mbar or a few tens of mbar. Few academic studies have been conducted with pressures exceeding 20 mbar. However, it has been observed that at extremely low pressures ($P < 1$ mbar), the deposition rate of the coating seems to increase with decreasing pressure [44].

The majority of experimental studies on ex-TEAB ("ex-" refers to the original precursor of the obtained coating.) coatings suggest the formation of a ternary B-C-N compound across diverse temperatures and operating conditions [44,46–49]. Adding ammonia has potential to decrease carbon concentration in CVD/LP-CVD [42,44,47,49,50] and PE-CVD coatings [42,46,51,52]. Carbon-free BN coatings were observed only in plasma enhanced

CVD (PE-CVD) coatings at high temperatures. Levy *et al*. [44] and Ramanuja [50] have defined two distinct coating regimes from TEAB, one with ammonia and one without. The inclusion of ammonia in the gas mixture restricts the presence of carbon contamination in high-temperature coatings by favoring the creation of hydrocyanic acid (HCN).

3.2. Thermodynamic calculations

Previous studies have focused on thermodynamic calculations under specific conditions for TEAB/N_2 and TEAB/NH_3/N_2 systems [53]. The authors examined the thermal decomposition of TEAB when mixed with nitrogen, with or without ammonia. The respective dilution ratios were $\alpha = 0$ and $\beta = 101$ for the TEAB/N_2 system and $\alpha = 16$ and $\beta = 5$ for the TEAB/NH_3/N_2 system. All computations were performed at 55 mbar, for both gaseous and solid species. The conclusion of the heterogeneous system indicates that the addition of ammonia improves hydrocarbon formation by providing extra hydrogen. Increased temperatures promote HCN production and decrease the amount of solid carbon. To restrict the carbon formation, limit homogeneous phase reactions and prevent pyrolysis of carbonaceous by-products such as C_2H_2 and CH_4, short residence times and cold wall CVD reactors are recommended in this study. Regarding the homogeneous system, both TEAB/N_2 and TEAB/NH_3/N_2 gas mixtures give similar results. The gas phase under 1200°C is mostly rich in hydrocarbons, whereas beyond that temperature, HCN, C_2H_2, low concentration of C_2H_4 and CH_3 and H radicals are produced. The introduction of NH_3 is equivalent to the addition of hydrogen, which favors saturated species and lighter hydrocarbons. Experimental gas analysis at the exit of a hot-wall CVD reactor revealed distinct TEAB decomposition modes. The production of gaseous carbon compounds, including HCN, CH_4, and C_2H_2, is at its maximum level when temperatures exceed 900°C and NH_3 is added. To efficiently remove carbon, primarily in the form of HCN and CH_4, during the LP-CVD experiments high temperatures seem to be necessary. The FTIR spectroscopy results are consistent with thermodynamic predictions, but kinetic effects also play a significant part. Solid carbon formation is indeed generally limited at short residence times, *i.e.*, at low precursor maturation. The study suggests that cold wall reactor could be used to reduce co-deposition of solid carbon [53]. By maintaining lower temperatures at the reactor walls, this reactor design would efficiently reduce the residence time of the precursor in the hot zone. The decomposition of the TEAB hydrocarbon branches, leading to reactive unsaturated species and eventually solid carbon, would therefore be limited.

The current study investigates the influence of several parameters on the formation of solid and gaseous phases from the TEAB/NH_3/N_2 system using a computational thermodynamic approach. These parameters include dilution coefficients α (0; 10; 20; 30; 60) and β (⅓; ½; 1; 2; 5), pressure (100; 200; 300; 400; 500 mbar) and temperature (400 to 2000°C). The primary objective is to enhance the knowledge of the relationship between these parameters and the formation of BN and to optimize these conditions for the elaboration of BN coatings with low carbon content. This approach requires a careful choice of dilution ratios, temperature, and pressure. This orchestration achieves the desired coating properties and kinetics, while advancing an understanding of the complex thermodynamic interactions of the CVD medium using this innovative precursor.

3.2.1. *Influence of dilution* $\alpha = {Q_{NH_3}}/{Q_{TEAB}}$

Thermodynamic calculations are carried out allowing the formation of a solid phase in addition to a gas phase. The dilution β is set equal to $1/3$ and the pressure is constant equal to 200 mbar. The dilution factor α varies between 0 and 60 (0; 10; 20; 30; 60), corresponding respectively to the TEAB/N_2 system ($\alpha = 0$) and TEAB/NH_3/N_2 ($\alpha = 60$, where the ammonia flow rate is 60 times greater than that of TEAB). The results of the thermodynamic calculations are shown in Figure 1. The mole fractions of gaseous and solid species are shown as a function of temperature and dilution ratio α. The curves for each species are represented by monochrome gradients symbolizing individual species according to color *i.e.*: N_2 in orange, CH_4 in blue, NH_3 in green, etc. The shade varies with the dilution factor α : the brightest corresponding to the lowest dilution: $\alpha = 0$ and conversely, the faintest corresponding to the highest dilution: $\alpha = 60$.

In this case, the addition of ammonia, *i.e.* $\alpha > 0$, decreases the mole fraction of methane (CH_4), thus reducing the carbon content in the coating. Conversely, hydrocyanic acid (HCN) appears only at high temperature. Hydrocyanic acid captures carbon atoms in the gaseous form and reduce the amount of solid carbon. In fact, The formation of HCN is to be promoted as much as possible in order to reduce the carbon content in the BN coating. Similarly, at 1000°C, the mole fraction of methane, a precursor of carbon coating, decreases, from 1.7×10^{-3} for $\alpha = 0$ to 9.7×10^{-4} for $\alpha = 10$, *i.e.* a reduction of over 40%. Increasing the value of the dilution α beyond 10 has no significant effect on the composition of the gas phase, except for the methane concentration, which remains constant at very low temperatures (while there is no carbon coating), then decreases progressively with increasing temperature. This transition is temperature-shifted: *e.g.* from 450°C for $\alpha = 10$ to 580°C for $\alpha = 60$. This shift corresponds to the start of methane decomposition in favor of solid carbon coating, which is also shifted at low temperatures by the addition of NH_3. The absence (or very low values < 10^{-6}) of boron species in the gas phase indicates that the majority of these boron species participate directly to the coating rather than to the creation of gaseous boron species.

Regarding the solid formation (cf. Figure 1.b, where "Gas" refers to the sum of all gaseous species detailed previously), graphite and boron nitride are the two thermodynamically stable phases. Boron nitride remains stable over the entire temperature and dilution range α, except in the absence of ammonia ($\alpha = 0$), for which boron nitride turns into boron carbide (B_4C) at around 1850°C. For the other dilutions, the higher nitrogen partial pressure stabilizes boron nitride up to 2000°C. Graphite remains relatively stable between 800 and 1800°C. Above 1800°C graphite feeds the gas phase with carbonaceous species (C_2H_6, C_2N_2), while between 400 and 800°C, the graphite mole fraction increases rapidly. Here again, the addition of ammonia drastically reduces the mole fraction of graphite at low temperatures, and its introduction in excess shifts the onset of the graphite phase in temperature. For example, graphite reaches a mole fraction equal to 1% at 470°C for $\alpha = 10$ versus 650°C for $\alpha = 60$. Increasing the dilution of TEAB in ammonia, and thus indirectly introducing an excess of nitrogen, delays the onset of formation of the graphite phase at temperature, by increasing the partial pressure of hydrocyanic acid and reducing that of methane. These results are in line with the literature, which suggests increasing the dilution ratio α to reduce the proportion of carbon in BN coatings.

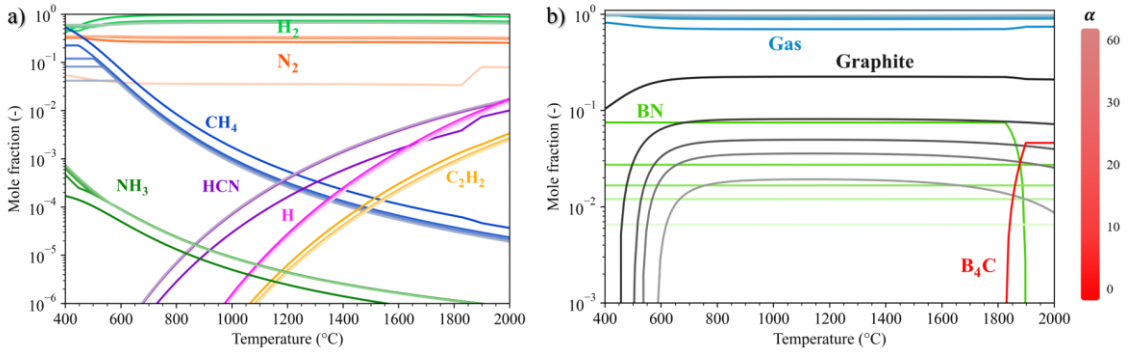

Figure 1 : Heterogeneous equilibrium mole fractions of a) gaseous species (H_2, N_2 CH_4, C_2H_2, HCN, NH_3 and H) and b) solid species (BN, C et B_4C for $\alpha = 0$ only) and gas for $\alpha = 0$; 10 ; 20 ; 30 and 60 ("Gas" refers to the sum of all gaseous species).

The driving forces for the formation of each solid phase, corresponding to the Gibbs free energy difference induced by the exclusion of the solid phases in the equilibrium calculations, normalized by $R.T$ (where R is the ideal gas constant and T is the temperature), are plotted as a function of temperature and α (cf. Figure 2). Here again, the addition of ammonia decreases the driving force for the graphitic carbon formation and simultaneously increases the BN formation for temperatures above 700°C. While the increase in α progressively reduces the driving force for solid carbon formation, the driving force for BN is globally unchanged. In order to obtain BN coatings with a minimum of carbon, it is therefore preferable to operate at a high α dilution ratio and at temperatures below 900°C. These conditions will certainly reduce the deposition kinetics, since increasing the dilution of TEAB in ammonia reduces the proportion of precursors in the gas mixture, while decreasing the reactor temperature slow down surface reactions.

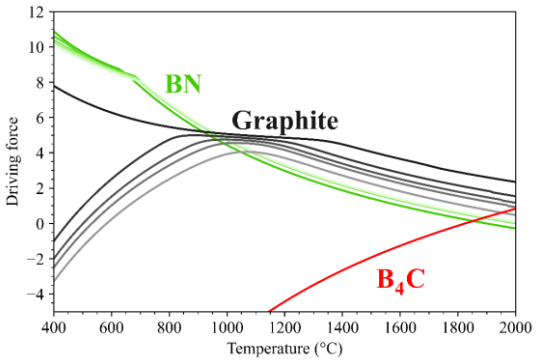

Figure 2 : Driving forces of solid species: C, BN (and B_4C for $\alpha = 0$ only) for $\alpha = 0$; 10 ; 20 ; 30 and 60.

3.2.2. *Influence of dilution* $\beta = Q_{N_2} / Q_{TEAB} + Q_{NH_3}$

Thermodynamic calculations are carried out by setting the α dilution ratio to 20 and the pressure to 200 mbar. The dilution factor β varies between ⅓ and 5 (⅓; ½; 1; 2; 5), *i.e.* in the TEAB/NH_3/N_2 system, with a nitrogen flow rate that is β times greater than that of TEAB+NH_3. The results of the thermodynamic calculations are gathered in Figure 3. The presentation of the results follows the same rules as before, with the shade this time providing information on the dilution factor β: the brightest corresponding to the lowest dilution: $\beta = ⅓$ and conversely, the faintest corresponding to the highest dilution: $\beta = 5$.

In this case, the species that are most affected by the variation in dilution β are H_2, N_2, CH_4, H, C_2H_2 and NH_3. Only hydrogen cyanide appears to be unaffected by the change in dilution. The mole fractions of the other species decrease as dilution increases, with a very slight temperature shift. For example: the proportion in methane drops from 500°C for $\beta = ⅓$, to 440°C for $\beta = 5$. Similarly, acetylene (C_2H_2) reaches a mole fraction of 10^{-5} at 1420°C for $\beta = ⅓$ versus 1320°C for $\beta = 5$. Increasing the dilution factor β has only a limited effect on the gas phase. On the other hand, increasing dilution β shifts the onset of methane decomposition and hence formation of free carbon. The gas phase remains stable for the lowest temperatures (< 500°C), then decreases as gaseous species contribute to the coating. The gas phase shows a minimum mole fraction between 1000 and 1150°C, indicating that most of the gas species participate in the coating. Beyond this point, the gas phase becomes again more abundant, to the detriment of the solid phase. In fact, the solid phase that varies in proportion in the graphitic carbon which, as the temperature rises, decomposes to form carbonaceous gas species. The mole fraction of BN is stable at all temperatures, while carbon vanishes at low temperatures (< 450°C), increases rapidly between 450°C and 1150°C, to reach a maximum, then gradually decreases up to 2000°C. It seems therefore preferable to choose the coating temperature away from this maximum in order to reduce the amount of free carbon in the solid. The lower the dilution β value, the higher the temperature of this maximum is. Finally, as expected, increasing the precursor dilution β leads to a decrease in the mole fractions of solid phases.

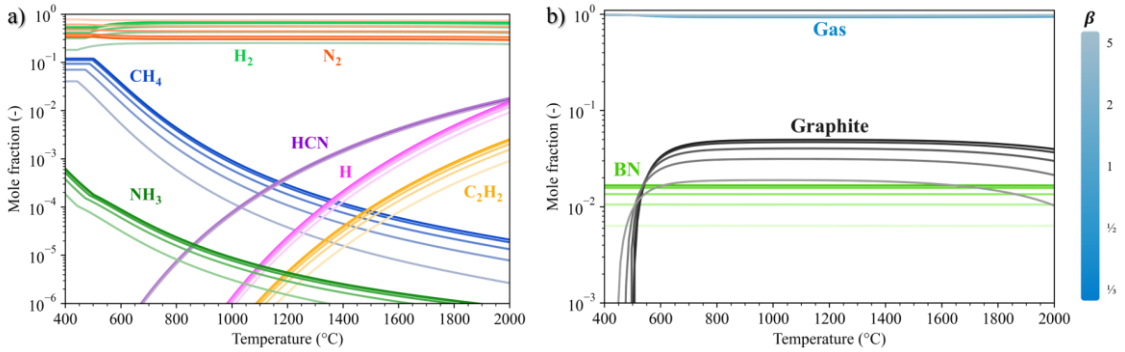

Figure 3 : Heterogeneous equilibrium mole fractions of a) gaseous species (H_2, N_2 CH_4, C_2H_2, HCN, NH_3 and H) and b) solid species (BN et C) for $\beta = {}^{1}/_{3}$; ${}^{1}/_{2}$; 1 ; 2 and 5 ("Gas" refers to the sum of all gaseous species).

For $\alpha = 20$, $\beta = ⅓$ and at 200 mbar, the ratio between the mole fraction of BN and graphite indicates that when the temperature increases from 500°C, the proportion of boron nitride decreases rapidly to reach a minimum equal to 25% at 1150°C, and then increases more slowly at higher temperatures. Here, in terms of BN proportion, the solid obtained at 800°C and 1600°C are equivalent and made of approximately 26% BN and 74% graphite.

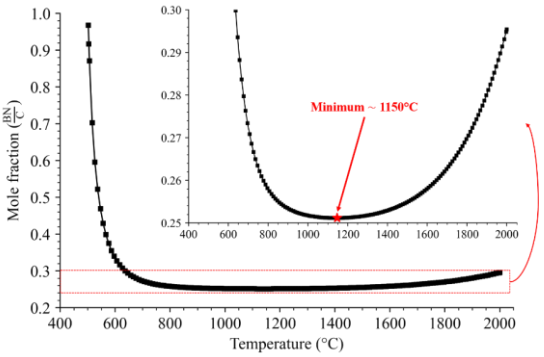

Figure 4 : Ratio of mole fractions between BN and C for $\alpha = 20$, $\beta = {}^{1}/_{3}$ and $P = 200$ mbar.

The driving forces of the solid species are plotted as a function of temperature and β dilution (cf. Figure 5). The driving force of boron nitride remains unchanged as a function of β and greater than that of carbon below 900°C. The variation in β influences both the value and the temperature shift of the maximum driving force of graphitic carbon. For example: the driving force of carbon becomes positive beyond 440°C for $\beta = ⅓$, versus 510°C for $\beta = 5$. It is therefore preferable to operate at a high β dilution to favor the BN phase, while possibly affecting the deposition rate.

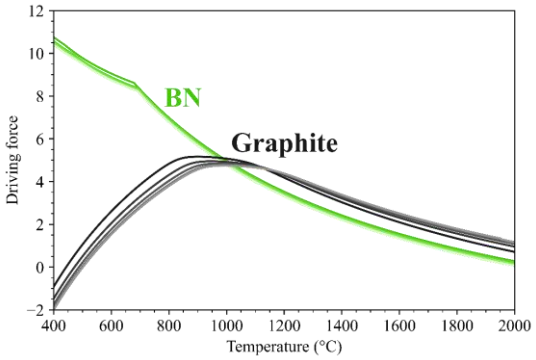

Figure 5 : Driving forces of solid species: C and BN for $\beta = {}^{1}/_{3}$; ${}^{1}/_{2}$; 1 ; 2 and 5.

3.2.3. Influence of pressure

In this section, thermodynamic calculations are carried out after setting the dilutions factors at $\alpha = 20$ and $\beta = ⅓$. The pressure in the reactor varies between 100 and 500 mbar (100; 200; 300; 400; 500 mbar). These levels of pressure are not usually encountered in the literature on the CVD of boron nitride since, generally, authors select lower pressures that are often more favorable in terms of coating quality or operations. However, the fluidized-bed technology requires higher pressures (> 100 mbar) for issues of fluidization quality and flow regimes. The results of the thermodynamic calculations are shown in Figure 6. The color gradation provides information on the pressure P *e.g.*: the brightest hue corresponds to the lowest pressure: $P = 100$ mbar whereas, the faintest hue relates to the highest dilution: $P = 500$ mbar.

For all the pressures explored here, the gas phase is made up of the same species as evidenced before. Pressure has no significant effect on the mole fractions of hydrocyanic acid and acetylene (all curves overlap, cf. Figure 5.a). On the other hand, raising the pressure increases the mole fraction of methane and ammonia, and decreases that of hydrogen (a shift to higher temperatures is observed for all curves). For example, the mole fraction of methane begins to fall at 460°C for 100 mbar, compared with 560°C for 500 mbar. This trend is also observed for graphite, which begins to appear at 460°C for 100 mbar and 560°C for 500 mbar. Conversely, hydrogen reaches a mole fraction of 10^{-3} at 1540°C for 100 mbar, versus 1640°C for 500 mbar. As before, the gas phase remains stable at the lowest temperatures (< 550°C), decreases rapidly to reach a minimum between 550°C and 1150°C, then increases again beyond 1150°C. At around 1950°C for $P = 100$ mbar, the proportion of the gas phase increases as BN disappears and boron carbide is formed. At other pressures, B_4C is absent over the temperature range studied. BN is stable at all pressures, while the appearance of graphite is temperature-shifted: it reaches 1% at 480°C for $P = 100$ mbar, versus 580°C for $P = 500$ mbar. At low temperatures (< 600°C), increasing the pressure favors the BN phase over graphite. However, after a certain temperature, the proportion of graphite increases very rapidly and the resulting coating contains more graphite than boron nitride.

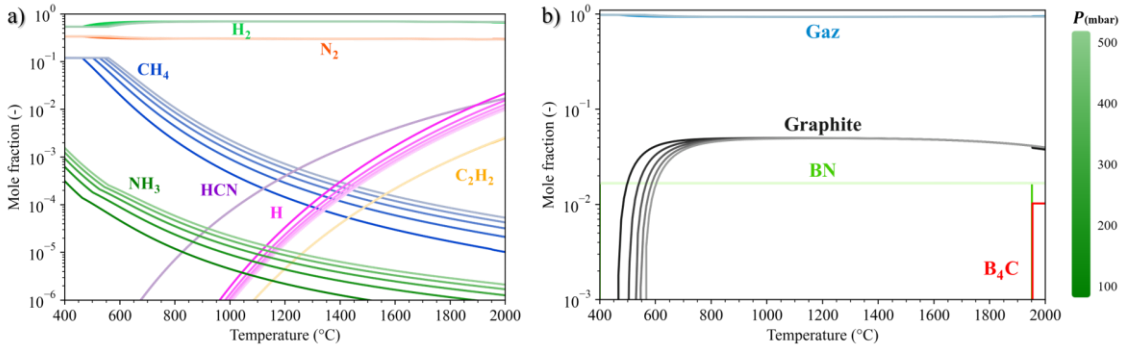

Figure 6 : Heterogeneous equilibrium mole fractions of a) gaseous species (H_2, N_2 CH_4, C_2H_2, HCN, NH_3 and H) and b) solid species (BN and C) for $P = 100$; 200 ; 300 ; 400 and 500 mbar.

The driving force of boron nitride changes very little with pressure. Below around 700°C, low pressures exhibit the highest BN driving forces, while above 700°C, the trend is reversed, and the highest BN driving forces are found at the highest pressures. For example, from 100 to 500 mbar, the driving force decreases by 5% at 500°C, while it increases by 7% at 900°C. The driving force of graphite is only affected below 1300°C. Increasing the pressure shifts the driving force of graphite to higher temperatures. Thus, increasing pressure delays the appearance of carbon in the BN coating.

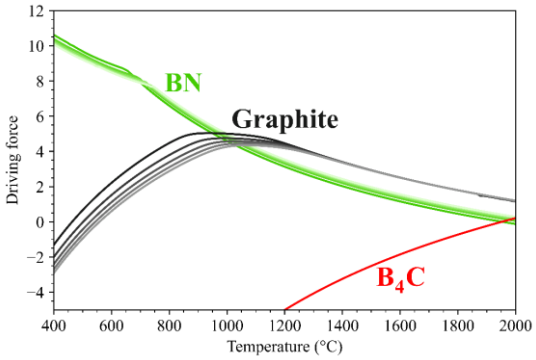

Figure 7 : Driving forces of solid species: C and BN for $P = 100$; 200 ; 300 ; 400 and 500 mbar.

3.3. FTIR study of the thermal decomposition of the TEAB/NH_3/N_2 system

The thermodynamic study provides an overview of the reaction products expected from the thermal decomposition of the precursor. Since this study is performed under conditions of thermodynamic equilibrium, experimental results may differ from theoretical data. During CVD coating, thermal decomposition of the gases is influenced by the residence time of the precursor species in the hot zone. This residence time is generally short, on the order of a few seconds at most. As a result, the in-situ partial pressures of the precursors and decomposition products do not reach a state of thermodynamic equilibrium, and the above calculations (that may differ from the hot gases generated in-situ) must be interpreted with caution.

This part of the research focuses specifically on the study of TEAB decomposition under different conditions using FTIR spectroscopy of cold exhaust gases of a specially designed CVD reactor. The preliminary thermodynamic approach revealed the importance of TEAB dilution in ammonia, obtained by adjusting the dilution ratio $\alpha = {Q_{NH_3}}/{Q_{TEAB}}$. Consequently, the dilution ratio α and the temperature were chosen as the key experimental parameters for this study.

It was decided to follow the relative variation of the concentrations of the species generated by the thermal decomposition of TEAB as a function of temperature, from ambient to 1000°C (the temperature limit of the reactor). The study was carried out at a pressure of 200 mbar, which is the pressure used for FB-CVD coatings. The reactor was cleaned between each manipulation and the spectra obtained in absorbance were corrected by subtracting the background spectrum (recorded without precursor diluted in nitrogen).

3.3.1. Variation in ammonia quantity

For each series of experiments ($\alpha = 0$, $\alpha = 10$ and $\alpha = 30$, shown in Figure 8), the operating parameters such as the total flow rate, pressure, and TEAB flow rate are held constant at values of 255 sccm, 2.5 sccm, and 200 mbar, respectively. The temperature of the bubbler water bath and the ammonia and nitrogen flow rates were adjusted to obtain the desired total flow rate and α dilution ratio.

The results are illustrated in Figure 8, which shows the FTIR spectra and the evolution of the areas under the peaks for each of the species for $\alpha = 0$, $\alpha = 10$ and $\alpha = 30$. For all α dilutions, at temperatures below 400°C, TEAB exhibits a characteristic infrared absorption band at 2400 cm^{-1}, due to the presence of the B-H bond, indicating the integrity of the complex. Above 400°C, this characteristic band is no longer observed and the triethylamine (TEA) characteristic absorption bands appear instead between 2750 and 3000 cm^{-1}. Above 600°C, new absorption bands appear corresponding to the formation of C_2H_4 and CH_4, indicating the onset of TEA decomposition. At even higher temperatures, the absorption bands of HCN and C_2H_2 are observed.

Experimental results show that methane, ethylene, and hydrocyanic acid exhibit a similar behavior. They appear at temperatures above 400°C and their sub-peak areas increase up to 800°C, before decreasing at higher temperatures. Acetylene, on the other hand, shows a continuous increase in the sub-peak area with increasing temperature up to 1000°C.

The infrared spectra obtained show a high intensity of ammonia absorption bands, with some of these bands even reaching saturation in the 500-1200 cm^{-1} region. These saturated bands overlap the absorption bands of other species in the 500-1700 cm^{-1} and 3200-3600 cm^{-1} ranges. At a temperature of 400°C, a distortion of the background appears, producing a peak around 3800 cm^{-1}. The results obtained do not show the appearance of new species with the addition of ammonia to the mixture.

The methane concentration increases between 400 and 1000°C, and this species is formed at lower temperature than in the TEAB/N_2 system. The sub-peak area for hydrocyanic acid increases from 600°C to 1000°C, while acetylene shows a similar trend in the TEAB/N_2 system. The addition of NH_3 has three effects on species formation, especially at elevated temperatures. First, it increases HCN production, which could lead to a potential decrease of the

amount of carbon in deposits formed at this temperature. Second, the partial pressure of CH_4 increases in the temperature range from 800 to 1000°C, which corresponds to an overall increase of carbon in the homogeneous phase. Finally, the presence of the NH_3 peaks makes impossible to process to the analysis of the C_2H_4 peak due to overlapping absorption bands between the two species.

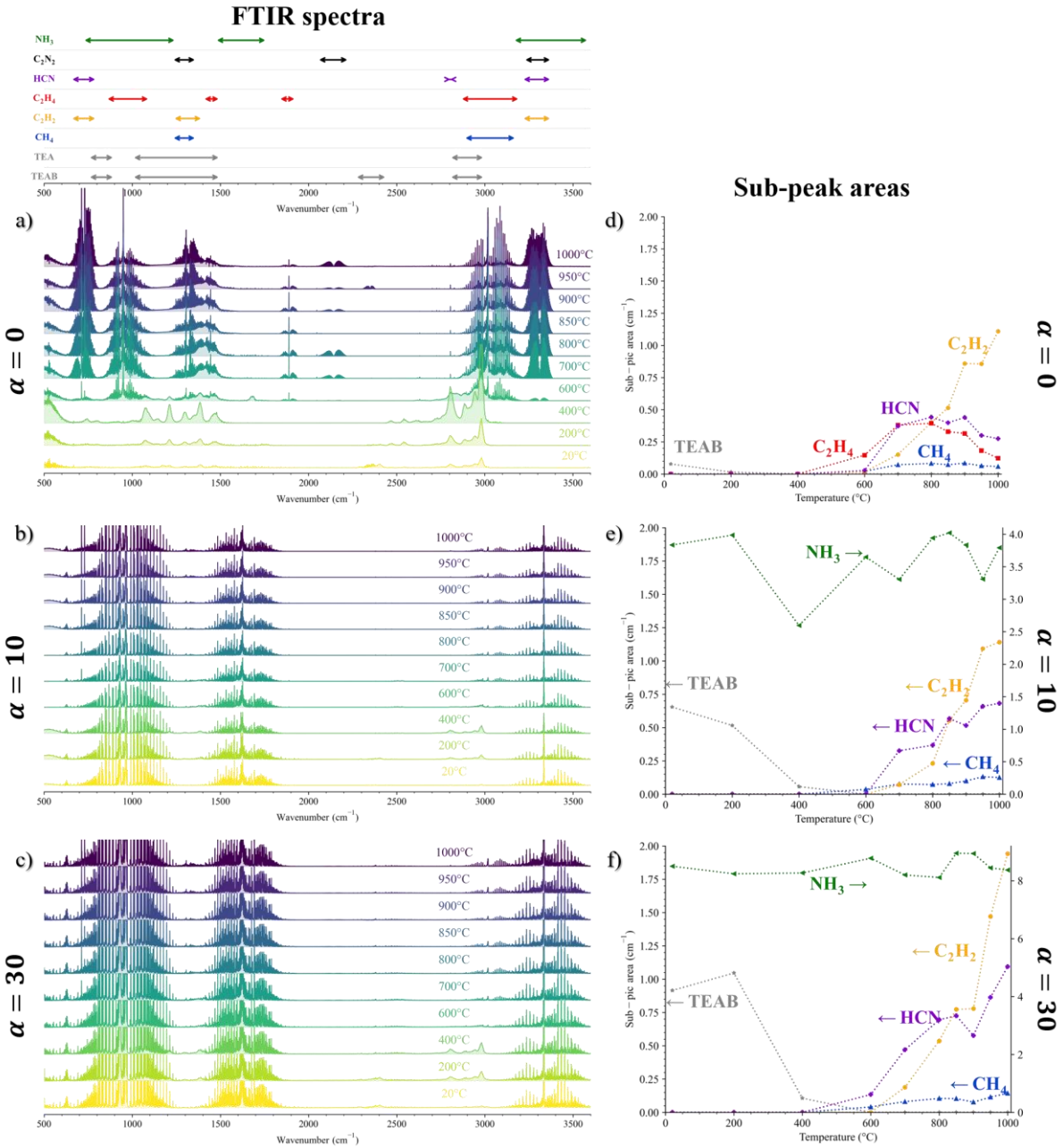

Figure 8 : FTIR spectra at different temperatures of the TEAB/NH_3/N_2 mixture at $P = 200$ mbar and $Q_{tot} = 255$ sccm. a) $\alpha = 0$, $\beta = 101$, b) $\alpha = 10$, $\beta = 8$ and c) $\alpha = 30$, $\beta = 2$. Sub-peak areas for the various species identified. d) $\alpha = 0$, $\beta = 101$, e) $\alpha = 10$, $\beta = 8$ and f) $\alpha = 30$, $\beta = 2$.

3.3.1. Comparison with thermodynamic study

Since thermal decomposition of the system during hot wall CVD occurs via both homogeneous and heterogeneous phase reactions (*i.e.*, leading to gaseous products and solid deposition), the results obtained from FTIR measurements are compared with both homogeneous and heterogeneous thermodynamic predictions at equilibrium. By preventing the formation of solid species (*i.e.*, assuming an infinite residence time of the gases), thermodynamic calculations predict the appearance of certain heavy species such as borazine ($B_3H_6N_3$) or benzene (C_6H_6), as well as other light borated species such as borane (BH_3) (see Figure S1 and S1 in Supplementary Material). However, these species are not revealed by FTIR measurements at the reactor outlet. Such a discrepancy between thermodynamic predictions and experimental measurements can be explained by the limited residence time of the gas

intermediates in the hot zone, or the high reactivity of certain species. The residence time under CVD conditions is limited to about half a second, which is not sufficient to allow the formation of high molecular weight species such as borazine or benzene that require significant molecular rearrangement relative to the initial precursors. Borane, on the other hand, is formed immediately after the B-N bond is broken in TEAB and does not require significant atomic rearrangement. Its absence in the FTIR spectra can therefore be attributed to its active contribution in the boron nitride deposition.

In contrast, the infrared spectra confirm the presence of methane (CH_4), acetylene (C_2H_2), ethylene (C_2H_4), and hydrogen cyanide (HCN), as predicted by thermodynamic calculations. The experimental results show that acetylene appears at temperatures above 600°C for $\alpha = 0$ and around 700°C for $\alpha = 10$, in agreement with thermodynamic predictions. According to the same predictions, the presence of CH_4 is expected over the entire temperature range for all α dilutions. However, for kinetic reasons, methane is experimentally detected only at 400°C and above. The fraction of ethylene increases up to 800°C for $\alpha = 0$ and then decreases at higher temperatures, contrary to thermodynamic predictions, which revealed a continuous increase over the whole temperature range. Finally, the experimental results show that the HCN onset temperature is lower than predicted for $\alpha = 0$ (600°C compared to 900°C for the thermodynamic prediction), but agrees for $\alpha > 0$, with a difference of about 20°C between FTIR results (700°C) and thermodynamic predictions (680°C). In conclusion, experimental measurements agree with thermodynamic calculations for light species that do not require significant molecular rearrangement, especially at high temperatures.

Theoretical and experimental studies therefore demonstrate that high α dilution ratio should minimize free carbon concentration in the BN coating. The β dilution ratio and the pressure are also helpful in reducing carbon concentration, although only of secondary importance. Temperature is a significant factor in controlling the carbon content, it is important to maintain a temperature that promotes effective decomposition of the precursor, typically around 400°C. However, it is crucial to avoid exceeding a range of 800-900°C, as this could lead to decomposition of ethyl groups and hence C and BN co-deposition. To decrease the carbon proportion within the coating, a higher α dilution appears to be appropriate. However, increasing the α dilution also reduces the concentration of TEAB in the gaseous precursor mixture, resulting in a very low deposition rate (less than ten nanometers per hour). In order to maintain a sufficient deposition rate, and given the need of regular flushing of the TEAB line (see section 2.1), the α dilution was set to 10. Due to the FB-CVD reactor technical constraints of heating and evaporation, and the requirements for the fluidization of the fibers/powder mixtures, it was chosen to synthesize a BN coating from TEAB at 800°C, 200 mbar, with a total gas flow of 250 sccm ($\sim 10U_{mf}$) and dilutions ratios of $\alpha = 10$ and $\beta = {}^{1}/_{3}$.

3.4. Characterization of the coatings

3.4.1. Global structure of the coating

The coated particles are observed by Scanning Electron Microscopy. Figure 9 shows secondary (SE) and backscattered electron (BSE) images. The images reveal the uniformity of the coating on the powder and fibers (cf. Figure 9.a). To better reveal the thickness of the coating, the particles were lightly flakked by hand with a mortar and observed under the same conditions (cf. Figure 9.b) showing a fiber with a slightly flaked coating, revealing the SiC substrate (brighter) and the BN coating (darker) by gray level contrast. The micrographs show that the coating is homogeneous on the surface of the powder and fibers, covering all particle asperities with the thickness in the order of a hundred nanometers. EDS was also carried out, confirming the presence of B, C, N, O and Si.

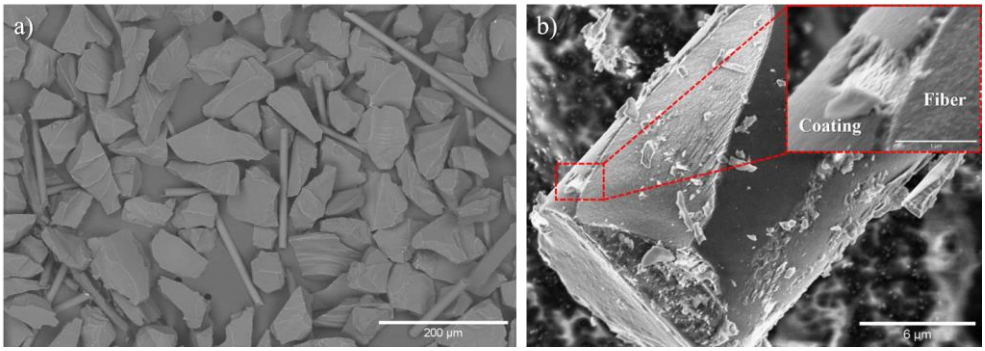

Figure 9 : a) SEM-BSE image showing homogeneously coated particles after the deposition process. b) SEM-SE image of the coating at the surface of a deliberately fractured fiber.

Preliminary SEM observations of the surface of the coated powders and fibers confirmed that the coating uniformly covers the particles. TEM cross-sectional analysis reveals that the coating thickness is approximately 100-110 nm (cf. Figure 10.a and Figure 10.b), regular from one particle to the next. The BN coating has an isotropic microstructure and is poorly crystallized. On the SAD pattern (cf. Figure 10.c), the signal associated with the first-order reflection of the sp^2-hybrided turbostratic BN (at $d_{002} \approx$ 0.3-0.4 nm) forms a diffuse and continuous circle, revealing that there is no preferential

orientation on the coating. The circle of bright spots corresponding to the 0.25 nm distance arise from the SiC nanograins (diffraction of the 111 planes of the cubic structure) of the Hi-Nicalon S fiber. The area selection diaphragm, with a diameter of 400 nm, includes both the thin coating and the fiber surface. The TEM-DF image (Figure 10.b) is low in contrast, homogeneous, and finely spotted at nanometric scale. The crystalline parameter L_c deduced from SAD pattern [38] is estimated at 2.5 nm. The HR-TEM image (Figure 10.d) shows coherent domains consisting of a stack of a few distorted basal layers less than five nanometers in size, corresponding to the small bright spots in the TEM-DF image (Figure 10.b). Such a poor structural organization is expected for BN prepared at low temperature [54,55]. In this study, the deposit was obtained in several stages, with interruptions in deposition and heating and intermediate atmospheric exposures. Remarkably, the coating presents no structural or chemical change and remains dense and homogeneous throughout his thickness.

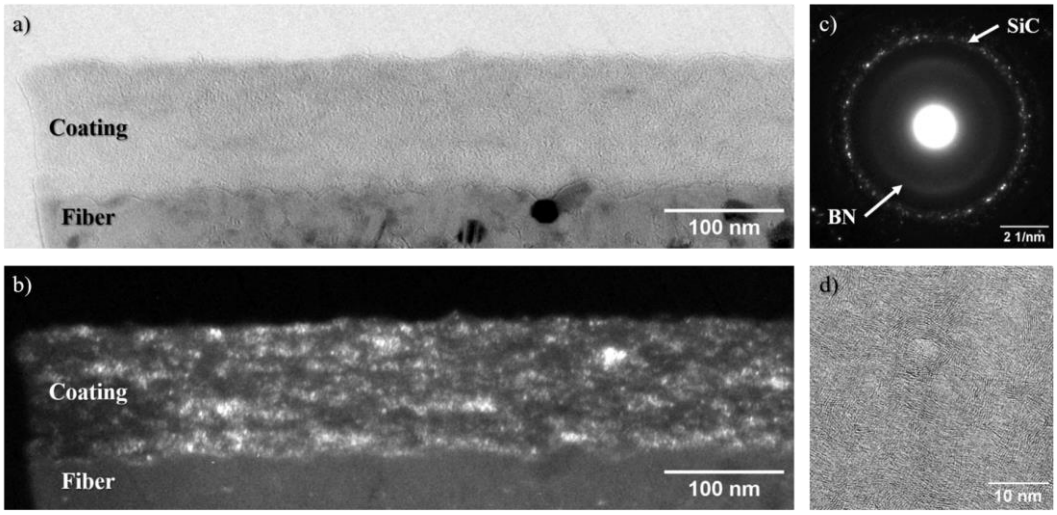

Figure 10 : TEM structural analysis of the coating: a) BF image, b) corresponding DF image, c) corresponding SAD pattern, d) HR image.

3.4.2. Global composition of the coating

After the final deposition stage, the FB-CVD coatings are stored under nitrogen to limit contamination from atmospheric moisture. The "thick" coating, cumulating 6 hours of deposition, is analyzed by Electron Energy Loss Spectroscopy. The EELS spectrum of the coating (cf. Figure 11) shows strong boron and nitrogen edges, but also reveals the presence of carbon and oxygen. The average atomic composition deduced from the area of the different characteristic edges is 41%$_{at.}$ of boron, 47%$_{at.}$ of nitrogen, 7%$_{at.}$ of oxygen and 5%$_{at.}$ of carbon. The shape of the B-K edge, with the two π^* and σ^* characteristics peaks at respectively 194 eV and 202 eV (cf. Figure 11 inset), similar as that of turbostratic boron nitride including carbon [54,56,57]. The EELS spectrum is therefore consistent with the microstructural description provided by TEM analysis. AES and XPS analysis confirm that the coating consists of boron nitride containing carbon and oxygen impurities.

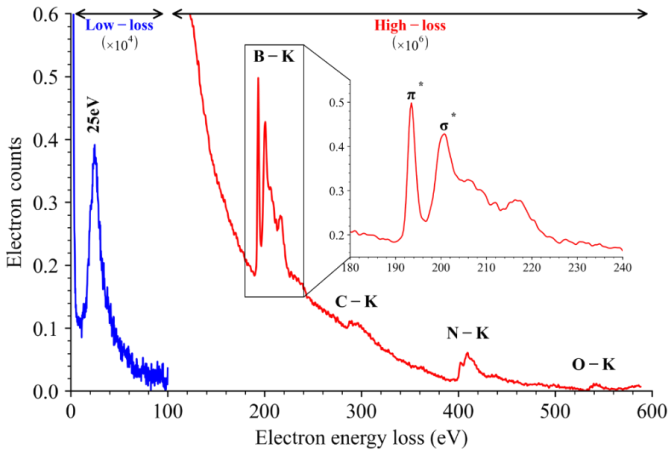

Figure 11 : Enlarged EELS spectrum and inset B-K edge.

The presence of carbon and oxygen impurities is often reported in poorly organized BN coatings obtained by CVD [54,56]. However, the amount of carbon present in this coating (5%$_{at.}$), derived from a precursor containing ethyl group, is notably low compared to that obtained for other CVD BN

coatings, about 25%$_{at.}$ for boron chloride/ammonia precursor [54] or 15%$_{at.}$ for boron-organic/ammonia precursor [56]. A careful investigation of carbon in the BN coating is necessary because it has been shown to alter its resistance to oxidation.

Auger Electron Spectroscopy, combined with ion etching, provides a much better spatial resolution compared to EDS, typically of a few nanometers. The particles are attached on a carbon scotch tape and placed under ultra-high vacuum in the analysis chamber. At the extreme surface of the fibers, zones of a few µm^2 are selected and progressively etched during the analysis. Figure 12.a shows the element tracking as a function of the sputter time. From the coating thickness measured by TEM, a sputter speed of approximatively 30 nm.min^{-1} can be deduced. After a thin layer of surface pollution (at zero sputter time), the coating turns out to be stoichiometric (average values of 48%$_{at.}$ of boron and 47%$_{at.}$ of nitrogen) with very low carbon and oxygen concentrations, around 3%$_{at.}$ and 2%$_{at.}$ respectively. Such an oxygen concentration is relatively low compared with others ex-BCl_3 BN coatings [25,37,58]. The low carbon concentration is even more remarkable considering the high carbon ratio of the precursor.

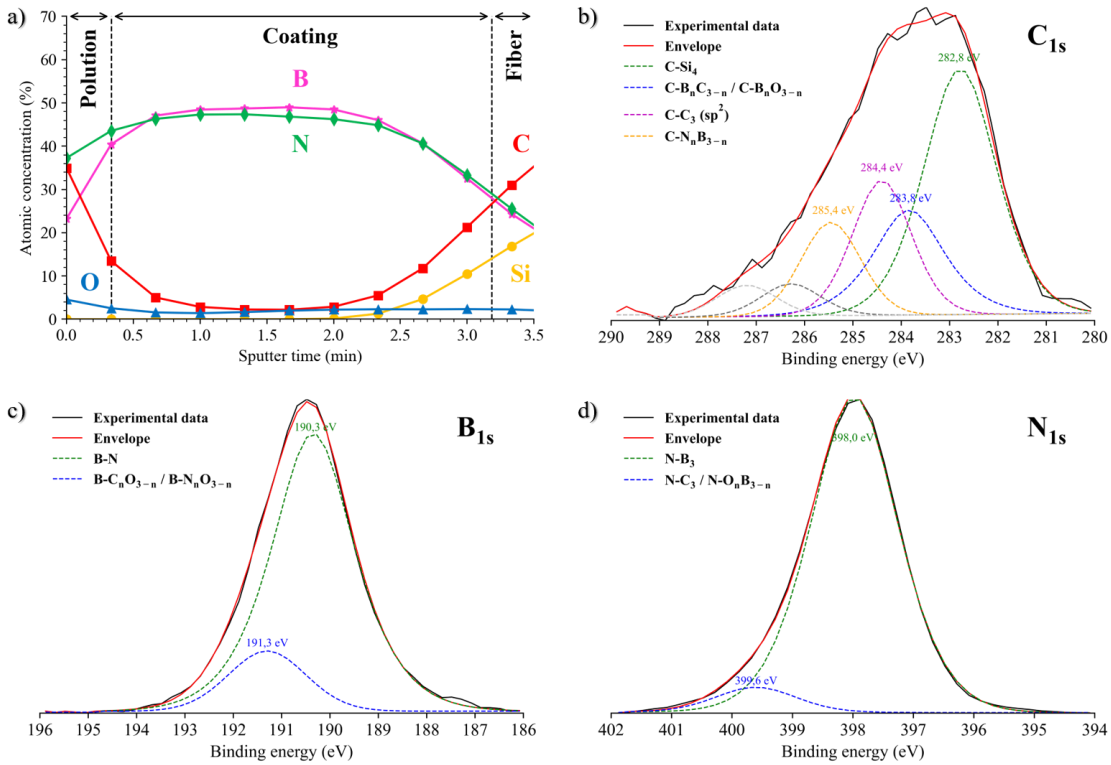

Figure 12 : a) Atomic concentration profile in the thickness obtained by AES. b), c) and d) XPS deconvolution of the C, B and N spectra obtained within the coating after sputtering.

XPS was used to characterize the chemical environment of the atoms in the coating. Figure 12.b, Figure 12.c and Figure 12.d present deconvolutions obtained from XPS spectra at the core of the deposit in the carbon, boron and nitrogen regions. The boron spectrum (B_{1s}, cf. Figure 12.c) shows predominantly B-N_3 bonds up to 39%$_{at.}$, and a less abundant boron bonds with carbon or oxygen up to 7%$_{at.}$. It should be noted that no component attributed to free boron, boron carbide (B_4C), or boron oxide (B_2O_3) were deduced from the deconvolution. The deconvolution of the nitrogen spectrum (N_{1s}, cf. Figure 12.d) shows a main peak at 398.0 eV, attributed to the N-B_3 environment (as in h-BN). This value is close to those commonly reported in the literature, around 398 eV [59]. However, other authors have reported shifts in this value for CVD BN deposits [37]. In contrast to Puyoo *et al.* results on ex-BCl_3 LP-CVD BN deposits, the ex-TEAB BN deposit reveals a nitrogen chemical environment consisting mainly of N-B_3 bonds. Puyoo *et al.* indeed observed several other components at higher energies, indicating a variety of atomic environments (N-B_2C, N-BC_2, N-C_3, and partially oxidized sites). The deconvolution of the carbon spectrum (C_{1s}, cf. Figure 12.b) shows a complex structure, reflecting a diversity of bonds formed by carbon. The peaks are centered around regions of C-B_n C_{3-n}, C-B_nO_{3-n}, and C-N_nB_{3-n} environments. A slight contribution from C-C_3 *sp²* bonds is observed around 284.4 eV. The chemical environment in the core of the BN coating is resumed in Table 2. The nitrogen region indicates a main *sp²* coordination with boron, while the carbon region suggests mixed *sp²* environments with nitrogen and boron. Finally, the oxygen atomic environment (not showed here) also suggests bonds with carbon, as well as hydrogen while the silicon environment is attributed to the Si-C bonds.

Table 2 : Summary of elements and chemical bonds detected by XPS with fit characteristics and atomic proportions.

Element/Bonding	Peak *(eV)*	FWHM *(eV)*	Area *(CPS.eV)*	Concentration *(%at.)*
B_{1s}	**189.70**	**2.17**	**31218.71**	**46.24**
BN	190.35	2.02	26255.87	39.08
BCO/BNO	191.30	1.89	4987.19	7.43
N_{1s}	**397.16**	**1.80**	**81599.37**	**37.31**
NB	397.97	1.70	75807.12	34.84
NC/NBO	399.61	1.55	5209.76	2.40
O_{1s}	**531.46**	**2.21**	**26424.08**	**8.20**
O=C	532.27	2.12	24024.82	7.50
O-C	534.29	1.47	1497.12	0.47
C_{1s}	**282.70**	**3.41**	**9458.34**	**7.21**
C-Si	282.78	1.77	3929.64	3.01
C-Si-O/C-B-C/C-B-O	283.84	1.73	1703.14	1.31
C-C (sp^2)	284.40	1.44	1733.89	1.33
C-N-B	285.45	1.46	1195.13	0.92
C-O-C	286.28	1.44	415.11	0.32
C=O	287.20	1.46	400.29	0.31
Si_{2p}	**99.82**	**2.36**	**1247.32**	**1.04**
Si-C	100.53	1.60	1223.49	1.03

3.4.3. Fiber/coating interface

In all cases the interface between the fiber and the coating observed in TEM is cohesive, the BN deposit adheres to the SiC surfaces of the powder and the fibers. At TEM high magnification, a nanometric amorphous phase, limited to a few nanometers in thickness, can be observed between the fiber and the coating (cf. Figure 13.a and Figure 13.b). In the STEM-HAADF mode (cf. Figure 13.a), the nanolayer appears discontinuous and irregular in thickness, with some contrast between the SiC fiber and the BN coating. The chemical composition profile line recorded by EELS trough the interface reveals that the amorphous phase contains oxygen and silicon (cf. Figure 13.c). At the interface, the Si-L_3 edge shifts slightly away from its position in the fiber (cf. Figure 13.d, comparison between (2) and (1) spectra). The peak value (107.5 eV) of the (2) spectrum suggests a Si-O type chemical environment in the interface [60]. The presence of this amorphous oxide layer can be attributed to the heat treatment of the desizing process of the fibers, during which the surface of the fibers is partially oxidized in air at 600°C. Advantageously, this amorphous phase at the interface does not appear to alter the coating ability adhesion to the fiber.

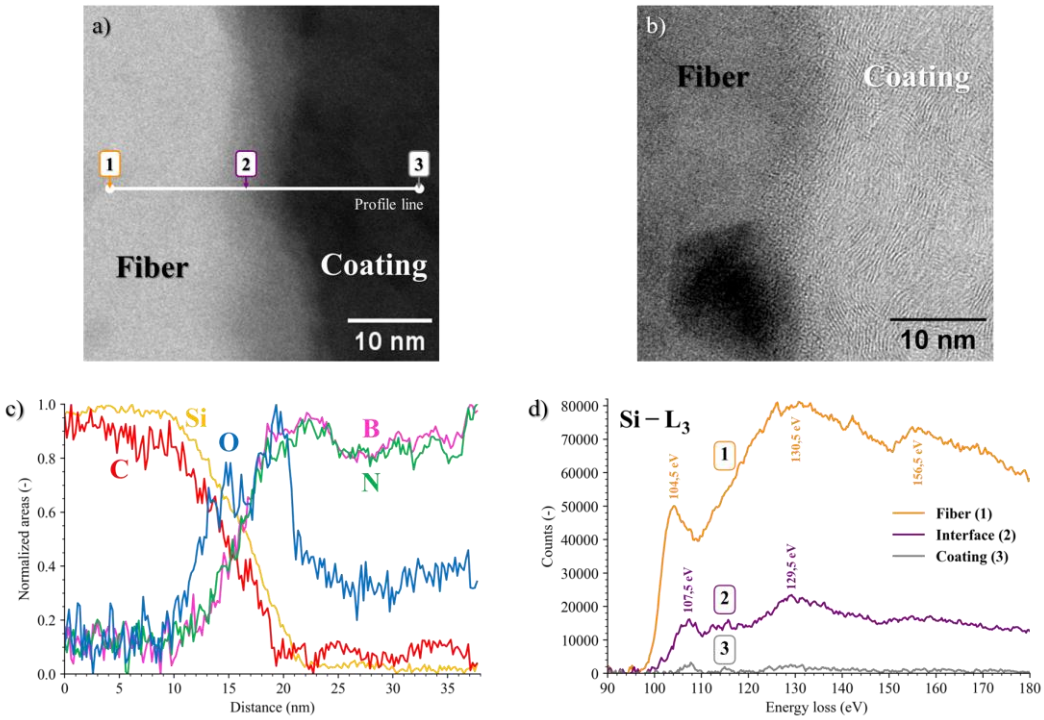

Figure 13 : Analysis of the fiber-coating interface: a) STEM-HAADF, b) HR-TEM images, c) normalized intensity of elements Si, C, B, N, O along profile line (white line in a) image). d) EELS Si-L$_3$ spectra in the fiber (1) at 0 nm, the interface (2) at 17 nm and the coating (3) at 38 nm (areas are marked on a) image).

3.4.4. Local coating characterizations

The STEM-HAADF imagery of the entire coating reveals uniformly dispersed dark nanometric regions (cf. Figure 14.a). Within the coating, on a more local scale, STEM-HAADF images show homogeneously distributed dark zones (cf. Figure 14.b). The STEM-BF image highlights a loss of the turbostratic structure at the dark and amorphous zones (cf. Figure 14.c). The EELS low-loss and core-loss spectra suggest a change in atomic density. Indeed, the EELS profile line through these local inhomogeneities indicates a variation in the intensity of the zero loss (ZL) peak, reflecting the evolution of the signal passing through the sample (see Figure S3 in Supplementary Material). At the center of the dark and amorphous zones, the ZL intensity increases, indicating a lower atomic density (*i.e.* more transmitted signal) compared to adjacent regions. This information can be interpreted in different ways. Assuming a uniform composition (*i.e.* a constant density), the variation in ZL intensity can be attributed to a variation in sample thickness. On the other hand, if a constant thickness is assumed, the variation in ZL intensity can be attributed to a variation in atomic density, meaning a variation in the elemental composition or structure of the material. At this stage of the analysis, it is not possible to determine the cause of this variation. However, it is possible to calculate, without further assumptions, the relative logarithmic ratio between thickness (t) and the mean free path of the electrons in the material (λ): $t/\lambda = -ln\left(I_0/I_t\right)$, also known as the mean number of scattering events per incident electron (see Figure S3 Supplementary Material). This quantity is proportional to the ratio of ZL intensities (I_0) to the sum of ZL and inelastic scattering (I_t). The darker regions show a significant decrease in the average scattering events per incident electron. While the light regions in STEM-HAADF imagery reflect areas of high atomic density, the dark regions correspond to a decrease in the average atomic density of the deposit.

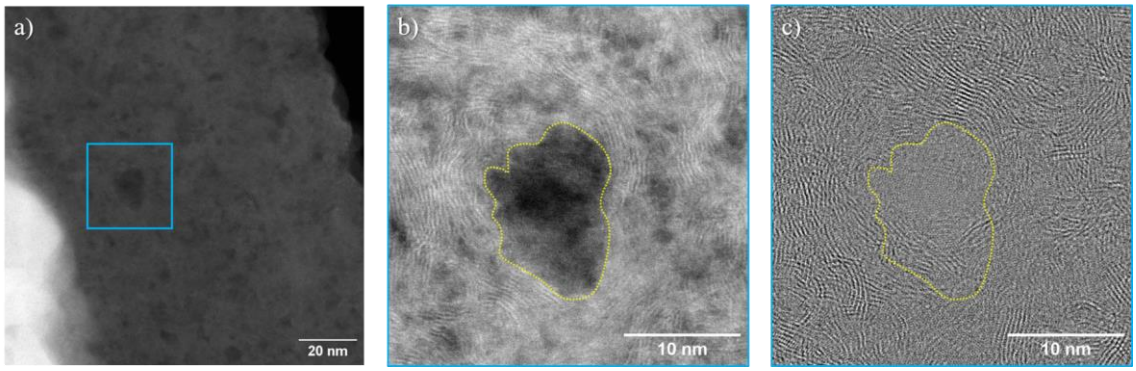

Figure 14 : a) Global STEM-HAADF of the BN coating (local inhomogeneity outlined in blue). b) STEM-HAADF and c) BF images of local inhomogeneity.

The EELS core-loss spectra show significant variation in the characteristic boron peaks as they pass through these dark zones (cf. Figure 15.a and Figure 15.b). Basically, during the ionization process, an electron in the electron cloud undergoes a transition from a *1s* core state to unoccupied states located in the conduction band above the Fermi level. These unoccupied states are specifically associated with orbitals of symmetry p_z (designated π^*) or p_x, p_y (designated σ^*). The boron K-edge spectrum illustrates the transitions between the *1s* core states and the π^* and σ^* states. These transitions appear on the EELS spectrum as two distinct peaks: one at around 194 eV corresponds to π^* transitions, while the other, at around 202 eV, corresponds to σ^* transitions. It is important to characterize these peaks, as their intensity, energy position, width and threshold energy reflect the projected density of states in the conduction band, *i.e.* the electronic, crystallographic and chemical environment. In hexagonal or turbostratic boron nitride materials, the intensities of these peaks are usually balanced [61–63,25,64] compared to pure σ-bonded materials like cubic boron nitride or boron carbide [65,41].

Recent studies of CVD-BN coatings on Nicalon fibers by Pippel *et al.* revealed the presence of chemically heterogeneous carbon-rich zones within the deposit [56]. Using energy-filtered elemental mapping (EFTEM), Pippel *et al.* observed the distribution of carbon and boron within the coating. Most of the carbon in the BN layer precipitates as nanoclusters (dark zones in HAADF images) between the BN nanocrystals. However, a comparison with other images revealed the presence of some carbon in the BN zones, possibly incorporated into the hexagonal BN structure.

For a better understanding of these results, the authors carried out a detailed analysis of the C-K edge. In contrast to the EELS spectrum of amorphous carbon, the carbon π^* peak in the BN coating is slightly more intense, and the σ^* peak sharper [56]. These observations indicate that the carbon in the coating is more graphitized than in an amorphous film. In addition, the appearance of the carbon peaks is shifted by around 2 eV compared with the reference spectrum of amorphous carbon. This difference can be interpreted by a lower binding energy of the carbon incorporated in BN(C), as the carbon atoms are surrounded by boron atoms with a lower electronegativity than carbon in graphite. This result is consistent with the composition profiles. In some regions of the coating, the difference between the boron and the nitrogen concentration cannot be compensated for by oxygen alone, suggesting the incorporation of carbon atoms to complete the hexagonal structure of BN. In our case, the carbon signal is too weak to characterize the π^* and σ^* peaks. However, the same methodology is used here for the boron peak.

The respective amplitudes of both π^* and σ^* peaks exhibit a variation along the profile as it passes through the inhomogeneity. At the edges of the dark zone spectrum (cf. Figure 15.c), the π^* peak (plotted in red) is more intense than the σ^* peak (plotted in green). This trend is inverted at the center of the zone (cf. Figure 15.d). To quantify this variation, two adjustments were made near these two peaks, using two Gaussian functions of the type: $y_{i,i=1,2} = {A_i}/{\sigma_i\sqrt{2\pi}} \; . exp\left({\left(x - x_{0_i}\right)^2}/{\sigma_i^2}\right)$. The first Gaussian, denoted 1, corresponds to the fit of the π^* peak, while the second Gaussian, denoted 2, corresponds to the fit on the σ^* peak. Figure 15.e shows the evolution of the parameter ${A_1\sigma_2}/{A_2\sigma_1}$, *i.e.* the ratio of the π^* and σ^* peak intensities.

Figure 15.e shows the variation in the boron ${\pi^*}/{\sigma^*}$ intensity ratio as a function of spatial position. This ratio is greater than 1 outside the darker regions and less than 1 within, indicating the loss of the turbostratic character within the darker zones. The organization of turbostratic BN is characterized by a balanced intensity of ${\pi^*}/{\sigma^*}$ (which corresponds to σ bonding within sp^2 layers and π bonding between adjacent layers). Conversely, a small ${\pi^*}/{\sigma^*}$ parameter typically corresponds to the presence of sp^3 bonding, as observed in structures such as boron carbide [66,67] or amorphous boron nitride [68] and BCN [66,69,70], which may occur between the basal sp^2 planes of turbostratic BN. The variation in ${t}/{\lambda}$ intensity is therefore mainly assignable to a change in material density.

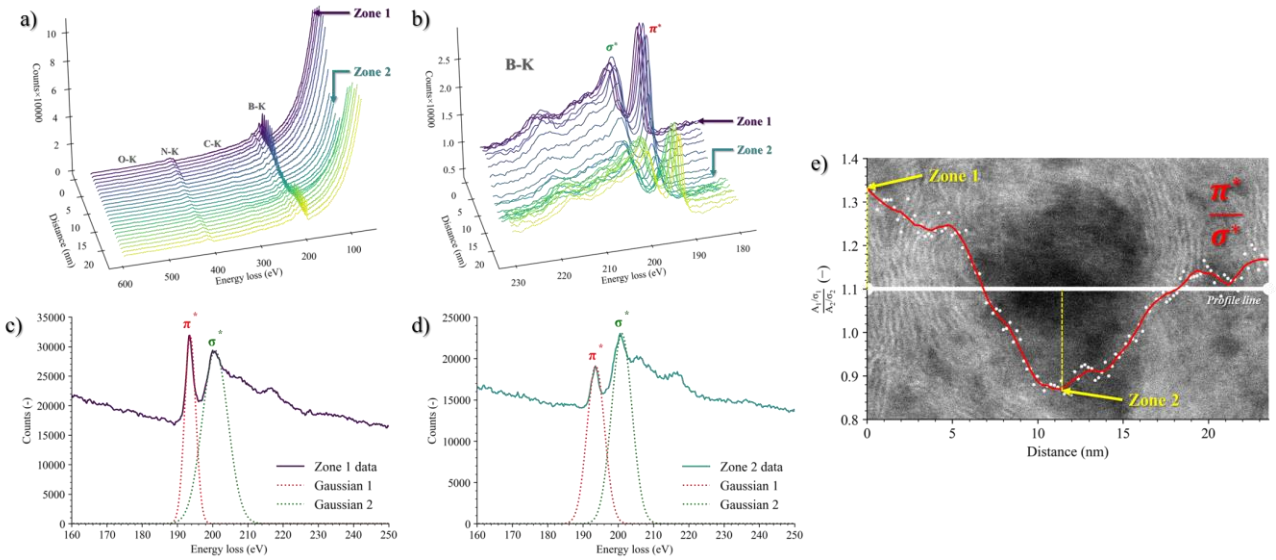

Figure 15 : a) EELS spectra and b) boron region along the profile line. Example of regression on a c) light (zone 1) and d) dark area (zone 2). e) π^*/σ^* ratio along the profile line.

The homogeneous elemental composition along the profile line is shown in Figure 16, this composition is consistent with the AES and XPS analysis. While boron and nitrogen concentrations remain stable along the profile line, and especially as they pass through these darker zones, oxygen and carbon concentrations tend to evolve in opposite directions. Outside these darker zones, oxygen dominates over carbon, while inside, carbon seems to dominate over oxygen. This trend may support the hypothesis that carbon is inserted into the BN structure and disrupts the turbostratic organization of the BN. Studies have indeed suggested that carbon insertion in the BN structure can distort hexagonal *sp²* planes, which can lead to a change in the $\pi^*/_{\sigma^*}$ parameter [61,71,72]. Considering that these zones of weak turbostratic organization are relatively richer in carbon than the rest of the deposit and that the deconvolutions of the XPS spectra indicate a majority of bonds between carbon and boron, it becomes very likely that the arrangement of covalent bonds in these zones becomes three-dimensional, as it can be in boron carbide for instance, which disturbs the turbostratic structure and explain the decrease in the $\pi^*/_{\sigma^*}$ parameter.

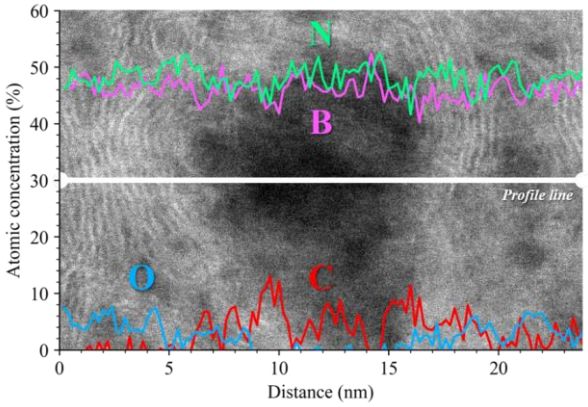

Figure 16 : STEM-HAADF image with profile line of elemental composition obtained by EELS.

In summary, this work indicates that: i) the majority of the carbon in the BN(C) deposit is arranged in the form of poorly organized nanoclusters (areas appearing dark on STEM-HAADF images and less organized on HR-TEM images) and ii) carbon is incorporated into the turbostratic BN structure, causing distortion of the *sp²* basal planes. The coating remains predominantly composed of turbostratic boron nitride, the main bonding being between boron and nitrogen atoms, with low carbon and oxygen concentrations. At the core of the deposit, disorganized carbon-rich structures of a few tens of nanometers are observed locally, which can be explained by the incorporation of carbon introduced during the precursor decomposition and deposition process. Electron Energy Loss Spectroscopy provides valuable information on the organization of the deposit and the distribution of carbon and oxygen heteroelements. The results of this analysis are consistent with previous studies of boron nitride coatings made with other precursors [54,56]. This feature is encouraging for the use of TEAB as a non-chlorinated second-generation precursor for stoichiometric BN coatings. Despite the presence of three ethyl

groups and a C:B ratio of 6:1, the coating retains a low atomic concentration of carbon and oxygen. In comparison, the atomic carbon contents observed by Pippel *et al.* [56] and Leparoux and Serin [54] were three and five times higher, respectively, than those analyzed here.

4. Conclusion

The thermodynamic study and experimental analysis of the gas phase highlighted the influence of certain CVD process parameters on the composition of the gases and solid phases resulting from TEAB decomposition, and in particular on the carbon content of the deposits. The α parameter ($\alpha = Q_{NH_3}/Q_{TEAB}$) appears as the most influential factor in reducing the carbon concentration in the coatings. High α values indeed promote the production of hydrocyanic acid (HCN), which reduces carbon contamination and favor the formation of pure boron nitride. Experimental examination of the thermal decomposition of TEAB precursor, via FTIR spectroscopy, confirmed the thermodynamic predictions and revealed the formation of new molecules such as methane (CH_4), acetylene (C_2H_2), ethylene (C_2H_4), and hydrogen cyanide (HCN) resulting from the precursor decomposition. The addition of ammonia into the reaction mixture enhances the formation of HCN, reducing the carbon content of the coatings (while the amount of carbonaceous species also increases with the initial ammonia concentration in the mixture).

In a second step, a comprehensive investigation of a low-carbon boron nitride coating has provided detailed information on its structure, microstructure and chemical composition. SEM imaging revealed the uniform coverage of all particles with an adherent coating of uniform thickness of approximately 100 nanometers. Assuming uniform deposition on all particle surfaces and stoichiometric deposition of h-BN, the yield of ex-TEAB deposition reaches around 50%, which is much higher than in the case of a BCl_3/NH_3 mixture (usually only a few percent). This result is mostly due to the FB-CVD process itself, which considerably favors mass transfer between the gas and the substrate. Elemental analysis confirmed the presence of boron, carbon, nitrogen and oxygen. TEM and EELS techniques were used to characterize the structure and chemical composition of the coating at the nanometer scale. The BN coating is isotropic and has a weakly crystallized structure, with coherent domains including several distorted basal layers, each measuring less than five nanometers. The EELS spectra unequivocally show the presence of boron, nitrogen, carbon, and oxygen. However, the carbon and oxygen content within the low-carbon ex-TEAB coating is significantly lower than in B-C-N coatings obtained other hydrocarbon containing precursors [37]. The carbon content is only $3\%_{at.}$ by AES spectroscopy ($5\%_{at.}$ by EELS spectroscopy). Such a concentration is not incompatible with the requirements for an application as a CMC interphase. B-C-N coatings with significantly higher carbon concentrations have indeed resulted in damage-resistant SiC/SiC composites and a much better oxidation resistance than pyrocarbon in dry air [37]. Nevertheless, as in the case of pure BN or carbon-rich B-C-N deposits, the wet corrosion resistance of the ex-TEAB BN deposit probably remains limited due to its poor structural organization [37,73]. Thermal post-treatments could further improve the chemical resistance by inducing BN recrystallization or at least a reorganization of the local environment of B atoms in the solid [37,43].

Acknowledgements

The authors wish to express their gratitude for the significant contributions of Sébastien Couthures and Rémi Bouvier in the maintenance of the fluidized bed reactor. A special appreciation is extended to Léane Da Calva for her work in processing thermodynamic data. The authors also thank the University of Bordeaux for granting financial support and Safran Ceramics for their operational assistance. Furthermore, the authors would like to acknowledge the contribution of Christine Labrugère and Mélanie Vaudescal from PLACAMAT for the X-ray Photoelectron Spectroscopy and Auger Electron Spectroscopy analysis.

Declaration of interests

The authors declare that they have no known competing financial interests or personal relationships that could have appeared to influence the work reported in this paper.

References

[1] Naslain RR. SiC-Matrix Composites: Nonbrittle Ceramics for Thermo-Structural Application. Int J Appl Ceram Technol 2005;2:75–84. https://doi.org/10.1111/j.1744-7402.2005.02009.x.

[2] Kerans RJ, Hay RS, Parthasarathy TA, Cinibulk MK. Interface Design for Oxidation-Resistant Ceramic Composites. J Am Ceram Soc 2002;85:2599–632. https://doi.org/10.1111/j.1151-2916.2002.tb00505.x.

[3] Pompidou S, Lamon J. Une condition de déviation des fissures dans les CMC et les multicouches. Comptes Rendus Mécanique 2005;333:405–11. https://doi.org/10.1016/j.crme.2005.03.001.

[4] Bokros JC. Variation in the crystallinity of carbons deposited in fluidized beds. Carbon 1965;3:201–11. https://doi.org/10.1016/0008-6223(65)90049-7.

[5] Bruggert M, Hu Z, Huttinger KJ. Chemistry and kinetics of chemical vapor deposition of pyrocarbon VI. influence of temperature using methane as a carbon source 1999:10.

[6] Burgio F, Fabbri P, Magnani G, Scafè M, Pilloni L, Brentari A, et al. Cf/C composites: correlation between CVI process parameters and Pyrolytic Carbon microstructure 2014:8.

[7] Ziegler I, Fournet R, Marquaire P-M. Influence of surface on chemical kinetic of pyrocarbon deposition obtained by propane pyrolysis. J Anal Appl Pyrolysis 2005:9.

[8] Hwang DG. Studies on the effects of the concentration in the preparation of C/C composites by the CVI process of propane. J Ind Eng Chem 2012:5.

[9] Becker A, Hüttinger KJ. Chemistry and kinetics of chemical vapor deposition of pyrocarbon — III pyrocarbon deposition from propylene and benzene in the low temperature regime. Carbon 1998;36:201–11. https://doi.org/10.1016/S0008-6223(97)00176-0.

[10] López-Honorato E, Meadows PJ, Xiao P. Fluidized bed chemical vapor deposition of pyrolytic carbon – I. Effect of deposition conditions on microstructure. Carbon 2009;47:251–62. https://doi.org/10.1016/j.carbon.2008.10.023.

[11] Lu C, Cheng L, Zhang L, Zhao C. Gas products and carbon deposition kinetics in chemical vapor deposition from propylene. New Carbon Mater 2010:5.

[12] Becker A, Hüttinger KJ. Chemistry and kinetics of chemical vapor deposition of pyrocarbon—II pyrocarbon deposition from ethylene, acetylene and 1,3-butadiene in the low temperature regime. Carbon 1998;36:177–99. https://doi.org/10.1016/S0008-6223(97)00175-9.

[13] Ghimire DC, Adhikari S, Aryal HR, Mominuzzamn SM, Soga T, Jimbo T, et al. Effects of ethylene gas flow rate on optoelectrical properties of nitrogenated thin amorphous carbon films grown by microwave surface wave plasma CVD 2008:4.

[14] Lai L-H, Huang K-J, Shiue S-T, Chang J-T, He J-L. Effects of Ethylene/Nitrogen Mixtures on Thermal Chemical Vapor Deposition Rates and Microstructures of Carbon Films. J Electrochem Soc 2012:9.

[15] Li W, Zhang S, Yan X, Li H, Li K. Densification and microstructure of carbon/carbon composites prepared by chemical vapor infiltration using ethanol as precursor. Sci China Technol Sci 2010;53:2232–8. https://doi.org/10.1007/s11431-009-3161-y.

[16] Li A, Zhang S, Reznik B, Lichtenberg S, Schoch G, Deutschmann O. Chemistry and kinetics of chemical vapor deposition of pyrolytic carbon from ethanol. Proc Combust Inst 2011;33:1843–50. https://doi.org/10.1016/j.proci.2010.06.037.

[17] Faggio G, Messina G, Lofaro C, Lisi N, Capasso A. Recent Advancements on the CVD of Graphene on Copper from Ethanol Vapor. C — J Carbon Res 2020;6:14. https://doi.org/10.3390/c6010014.

[18] Da Calva Mouillevois T, Rivière C, Chollon G, Vignoles G, Bertrand N. Gaseous fluidization of short fibers and powders, influence of temperature and pressure. Chem Eng J 2023;453:139612. https://doi.org/10.1016/j.cej.2022.139612.

[19] Jacques S, Lopez-Marure A, Vincent C, Vincent H, Bouix J. SiC/SiC minicomposites with structure-graded BN interphases. J Eur Ceram Soc 2000;20:1929–38. https://doi.org/10.1016/S0955-2219(00)00064-9.

[20] Cofer CG, Economy J. Oxidative and hydrolytic stability of boron nitride — A new approach to improving the oxidation resistance of carbonaceous structures. Carbon N Y 1995;33:389–95. https://doi.org/10.1016/0008-6223(94)00163-T.

[21] Jacobson N, Farmer S, Moore A, Sayir H. High Temperature Oxidation Behavior of Boron Nitride Part I: Monolithic BN. J Am Ceram Soc 1999;82:393–8.

[22] Pavlović V, Kötter H-R, Meixner C. Chemical vapor deposition of boron nitride using premixed borontrichloride and ammonia. J Mater Res 1991;6:2393–6. https://doi.org/10.1557/JMR.1991.2393.

[23] Patibandla N, Luthra KL. Chemical Vapor Deposition of Boron Nitride. J Electrochem Soc 1992;139:3558–65. https://doi.org/10.1149/1.2069121.

[24] Cholet V, Vandenbulcke L. Chemical Vapor Infiltration of Boron Nitride Interphase in Ceramic Fiber Preforms: Discussion of Some Aspects of the Fundamentals of the Isothermal Chemical Vapor Infiltration Process. J Am Ceram Soc 1993;76:2846–58. https://doi.org/10.1111/j.1151-2916.1993.tb04026.x.

[25] Le Gallet S, Chollon G, Rebillat F, Guette A, Bourrat X, Naslain R, et al. Microstructural and microtextural investigations of boron nitride deposited from BCl3–NH3–H2 gas mixtures. J Eur Ceram Soc 2004;24:33–44. https://doi.org/10.1016/S0955-2219(03)00126-2.

[26] Prouhet S, Guette A, Langlais F. An Experimental Kinetic Study Of Boron Nitride CVD From BF_3-NH_3-Ar Mixtures. J Phys IV 1991;02:C2-119-C2-126. https://doi.org/10.1051/jp4:1991214.

[27] Rebillat F, Guette A, Nasiain R, Brosse CR. Highly ordered pyrolytic BN obtained by LPCVD. J Eur Ceram Soc 1997;17:1403–14. https://doi.org/10.1016/S0955-2219(96)00244-0.

[28] Jacques S, Vincent H, Vincent C, Lopez-Marure A, Bouix J. Multilayered BN Coatings Processed by a Continuous LPCVD Treatment onto Hi-Nicalon Fibers. J Solid State Chem 2001;162:358–63. https://doi.org/10.1006/jssc.2001.9387.

[29] Da Calva Mouillevois T, Audren-Paul M, Chollon G, Bertrand N. Fluidization of variable short fiber/powder mixtures: Hydrodynamic investigation. Chem Eng J 2023:144846. https://doi.org/10.1016/j.cej.2023.144846.

[30] El Mansouri A, Bertrand N, Couthures S, Guette A. Apparatus for Fluidized-Bed Chemical Vapour Deposition. WO2022003268 (A1), 2022.

[31] Andersson J-O, Helander T, Höglund L, Shi P, Sundman B. Thermo-Calc & DICTRA, computational tools for materials science. Calphad 2002;26:273–312. https://doi.org/10.1016/S0364-5916(02)00037-8.

[32] Saunders N, Miodownik AP. CALPHAD (Calculation of Phase Diagrams): A Comprehensive Guide. vol. 52. New York: Elsevier; 1998.

[33] Lukas HL, Fries SG, Sundman B. Computational thermodynamics: the CALPHAD method, 2007. N Y Camb Univ n.d.

[34] Thomas C. Allison. NIST-JANAF Thermochemical Tables - SRD 13 2013. https://doi.org/10.18434/T42S31.

[35] McBride BJ. NASA Glenn Coefficients for Calculating Thermodynamic Properties of Individual Species. National Aeronautics and Space Administration, John H. Glenn Research Center at Lewis Field; 2002.

[36] Duschanek H, Rogl P, Lukas H. A critical assessment and thermodynamic calculation of the boron-carbon-titanium (BC-Ti) ternary system. J Phase Equilibria 1995;16:46–60.

[37] Puyoo G, Teyssandier F, Pailler R, Labrugère C, Chollon G. Boron carbonitride coatings synthesized by LPCVD, structure and properties. Carbon 2017;122:19–46. https://doi.org/10.1016/j.carbon.2017.06.024.

[38] Bourrat X, Trouvat B, Limousin G, Vignoles G, Doux F. Pyrocarbon anisotropy as measured by electron diffraction and polarized light. J Mater Res 2000;15:92–101. https://doi.org/10.1557/JMR.2000.0017.

[39] Scherrer P. Bestimmung der Grosse und inneren Struktur von Kolloidteilchen mittels Rontgenstrahlen. Nach Ges Wiss Gottingen 1918;2:8–100.

[40] Desenfant A. Dépôt chimique en phase vapeur (CVD) de carbure de silicium (SiC) à partir de vinyltrichlorosilane (VTS) et de méthylsilane (MS) n.d.:251.

[41] Huang J-L, Pan C-H, Lii D-F. Investigation of the BN films prepared by low pressure chemical vapor deposition. Surf Coat Technol 1999;122:166–75. https://doi.org/10.1016/S0257-8972(99)00306-0.

[42] Kosinova ML, Fainer NI, Rumyantsev YuM, Golubenko AN, Kuznetsov FA. LPCVD boron carbonitride films from triethylamine borane. J Phys IV 1999;09:Pr8-915-Pr8-921. https://doi.org/10.1051/jp4:19998115.

[43] Carminati P. Composites SiC/SiC à interphase de type BN de compositions variables et réactivité optimisée n.d.:270.

[44] Levy RA, Mastromatteo E, Grow JM, Paturi V, Kuo WP, Boeglin HJ, et al. Low pressure chemical vapor deposition of B-N-C-H films from triethylamine borane complex. J Mater Res 1995;10:320–7. https://doi.org/10.1557/JMR.1995.0320.

[45] Shayapov VR, Kosinova ML, Smirnov AP, Maksimovskii EA, Ayupov BM, Rumyantsev YuM. Mechanical properties and density of BC_xN_y films grown by low-pressure chemical vapor deposition from triethylamine borane. Inorg Mater 2011;47:262–6. https://doi.org/10.1134/S0020168511030204.

[46] Hoffmann PS, Baake O, Kosinova ML, Beckhoff B, Klein A, Pollakowski B, et al. Chemical bonds and elemental compositions of BC_xN_y layers produced by chemical vapor deposition with trimethylamine borane, triethylamine borane, or trimethylborazine: Chemical identification by XPS and TXRF-NEXAFS. X-Ray Spectrom 2012;41:240–6. https://doi.org/10.1002/xrs.2387.

[47] Grow JM, Levy RA. Micromechanical characterization of chemically vapor deposited ceramic films. J Mater Res 1994;9:2072–8. https://doi.org/10.1557/JMR.1994.2072.

[48] Thamm T, Körner K-U, Bohne W, Strub E, Röhrich J, Stöckel S, et al. Characterization of PECVD boron carbonitride layers. Appl Surf Sci 2005;252:223–6. https://doi.org/10.1016/j.apsusc.2005.02.041.

[49] Baake O, Hoffmann PS, Kosinova ML, Klein A, Pollakowski B, Beckhoff B, et al. Analytical characterization of BC_xN_y films generated by LPCVD with triethylamine borane. Anal Bioanal Chem 2010;398:1077–84. https://doi.org/10.1007/s00216-010-3965-4.

[50] Ramanuja N. Low pressure chemical vapor deposition of boron nitride thin films from triethylamine borane complex and ammonia. Theses 1998.

[51] Rohr C, Boo J-H, Ho W. The growth of hexagonal boron nitride thin films on silicon using single source precursor. Thin Solid Films 1998;322:9–13. https://doi.org/10.1016/S0040-6090(97)01007-9.

[52] Merenkov IS, Kasatkin IA, Maksimovskii EA, Alferova NI, Kosinova ML. Vertically aligned layers of hexagonal boron nitride: PECVD synthesis from triethylaminoborane and structural features. J Struct Chem 2017;58:1018–24. https://doi.org/10.1134/S0022476617050237.

[53] Fenetaud P, Roger J, Chollon G, Jacques S. Triethylamine borane thermal decomposition for BN low pressure chemical vapour deposition. Surf Coat Technol 2023;472:129927. https://doi.org/10.1016/j.surfcoat.2023.129927.

[54] Leparoux M, Vandenbulcke L, Clinard C. Influence of Isothermal Chemical Vapor Deposition and Chemical Vapor Infiltration Conditions on the Deposition Kinetics and Structure of Boron Nitride. J Am Ceram Soc 1999;82:1187–95. https://doi.org/10.1111/j.1151-2916.1999.tb01894.x.

[55] Plaisantin H, Jacques S, Danet J, Camus G, Delpouve H. TEM characterization of turbostratic and rhombohedral BN interphases synthesized by chemical vapour infiltration in SiC/SiC-Si composites. Mater Charact 2021;172:110857. https://doi.org/10.1016/j.matchar.2020.110857.

[56] Pippel E, Woltersdorf J, Dietrich D. CVD-coated boron nitride on continuous silicon carbide ®bres: structure and nanocomposition. J Eur Ceram Soc 2000.

[57] Li D, Yu D, Wang P, Li Y, He J, Xu B, et al. Crystallization of an amorphous B–C–N precursor with a Li–B–N catalyst at high pressures and temperatures. Mater Charact 2009;60:1411–4. https://doi.org/10.1016/j.matchar.2009.06.001.

[58] Dai J, Wang Y, Xu Z, Mu R, He L. Influence of hydrogen on growth and microstructure of boron nitride coatings obtained from BCl3–NH3–H2 system by chemical vapor infiltration. Ceram Int 2020;46:13073–81. https://doi.org/10.1016/j.ceramint.2020.02.078.

[59] Saugnac F, Teyssandier F, Marchand A. Characterization of C-B-N Solid Solutions Deposited from a Gaseous Phase between 900° and 1050°C. J Am Ceram Soc 1992;75:161–9. https://doi.org/10.1111/j.1151-2916.1992.tb05459.x.

[60] Batson PE. Current trends for EELS studies in physics. Microsc Microanal Microstruct 1991;2:395–402. https://doi.org/10.1051/mmm:0199100202-3039500.

[61] Schmid HK. Phase Identification in Carbon and BN Systems by EELS. Microsc Microanal Microstruct 1995;6:99–111. https://doi.org/10.1051/mmm:1995110.

[62] Saulig-Wenger K, Cornu D, Chassagneux F, Ferro G, Epicier T, Miele P. Direct synthesis of b-SiC and h-BN coated b-SiC nanowires. Solid State Commun 2002.

[63] Chen L, Ye H, Gogotsi Y, McNallan MJ. Carbothermal Synthesis of Boron Nitride Coatings on Silicon Carbide. J Am Ceram Soc 2003;86:1830–7. https://doi.org/10.1111/j.1151-2916.2003.tb03568.x.

[64] Olovsson W, Magnuson M. Rhombohedral and Turbostratic Boron Nitride Polytypes Investigated by X-ray Absorption Spectroscopy. J Phys Chem C 2022;126:21101–8. https://doi.org/10.1021/acs.jpcc.2c06895.

[65] Jaouen M, Hug G, Gonnet V, Demazeau G, Tourillon G. An EELS and XAS Study of Cubic Boron Nitride Synthesized under High Pressure - High Temperature Conditions. Microsc Microanal Microstruct 1995;6:127–39. https://doi.org/10.1051/mmm:1995113.

[66] Garvie LAJ, Hubert H, Petuskey WT, McMillan PF, Buseck PR. High-Pressure, High-Temperature Syntheses in the B–C–N–O System. J Solid State Chem 1997;133:365–71. https://doi.org/10.1006/jssc.1997.7583.

[67] Oyama T, Takeuchi K. Gas-phase synthesis of crystalline B4C encapsulated in graphitic particles by pulsed-laser irradiation. Carbon 1999;37:433–6. https://doi.org/10.1016/S0008-6223(98)00209-7.

[68] Suzuki S, Tomita M, Takayoshi Hayashi TH. Electron Energy Loss Spectroscopy of Amorphous Boron Filaments. Jpn J Appl Phys 1995;34:L191. https://doi.org/10.1143/JJAP.34.L191.

[69] Leardini F, Flores E, E ARG, Ferrer IJ, Ares JR, Sánchez C, et al. Chemical vapor deposition growth of boron–carbon–nitrogen layers from methylamine borane thermolysis products. Nanotechnology 2017;29:025603. https://doi.org/10.1088/1361-6528/aa9c07.

[70] Leardini F, Jiménez-Arévalo N, Ferrer IJ, Ares JR, Molina P, Navarro CG, et al. A fast synthesis route of boron–carbon–nitrogen ultrathin layers towards highly mixed ternary B–C–N phases. 2D Mater 2019;6:035015. https://doi.org/10.1088/2053-1583/ab175c.

[71] Caretti I, Torres R, Gago R, Landa-Cánovas AR, Jiménez I. Effect of Carbon Incorporation on the Microstructure of BCxN (x = 0.25, 1, and 4) Ternary Solid Solutions Studied by Transmission Electron Microscopy. Chem Mater 2010;22:1949–51. https://doi.org/10.1021/cm9038472.

[72] McDougall NL, Partridge JG, Nicholls RJ, Russo SP, McCulloch DG. Influence of point defects on the near edge structure of hexagonal boron nitride. Phys Rev B 2017;96:144106. https://doi.org/10.1103/PhysRevB.96.144106.

[73] Carminati P, Jacques S, Rebillat F. Oxidation/corrosion of BN-based coatings as prospective interphases for SiC/SiC composites. J Eur Ceram Soc 2021;41:3120–31. https://doi.org/10.1016/j.jeurceramsoc.2020.07.056.

Vitae

765

Thomas Da Calva Mouillevois is a Ph.D. graduate from the University of Bordeaux. He is working on the development of ceramic coatings and short fibers fluidization at the ThermoStructural Composites Laboratory since 2020. Graduated from the National Engineering School of Tarbes, France in the speciality of Structural Materials and Processes Engineering, Thomas Da Calva also holds a double degree in Materials Processing Characterization and Surface Treatments in partnership with the National School of Chemical and Technological Arts Engineers and the Paul Sabatier University of Toulouse.

Clément Rivière holds a master's degree in chemistry, specializing in advanced materials, from the University of Bordeaux. Throughout his training, he extensively explored composite materials. During his 6-month internship at LCTS, he focused on the thermal decomposition of liquid precursors by CVD. With a profound interest for materials engineering, he aspires to build a career in the realm of motorsports material engineering.

Hervé Plaisantin is research ingenior at SAFRAN since 2000. He graduated from the National Superior Ingenior School of Caen in 1994 and obtained a Ph.D in Materials Science from the University of Bordeaux in 1999. Since 2005, he has been working at the LCTS on the development of materials and processes developed by SAFRAN for aeronautical applications. He currently specializes in the microstructural characterization of ceramic phases (boron nitride, silicon carbide, carbon), especially by Transmission Electron Microscopy.

Jérôme Roger is an Assistant Professor in the Chemistry Department of the University of Bordeaux since 2011. He obtained a Ph.D. in solid state chemistry in 2005 at the University of Rennes 1. His main topics of interest concern the synthesis and the characterization of high temperature ceramics and their thermodynamics. Her current research activities focus on the synthesis of innovative SiC-rich matrices for CMCs.

Teresa Hungria is material characterization engineer at Raimond Castaing Microcharacterization Center, University of Toulouse (France) since 2013. She obtained a Ph.D in physical chemistry in 2005 at the Autonomous University of Madrid (Spain). She is currently a specialist in material characterization using SIMS and high resolution TEM/STEM analysis coupled with EDS and EELS.

Georges Chollon is research scientist at the French National Center for Scientific Research (CNRS) since 1999. He graduated from the National School of Physics and Chemistry of Bordeaux in 1990 and obtained a Ph.D. in Materials Science from the University of Bordeaux in 1995. He completed two post-doctoral fellowships, at EMPA-Dübendorf, Switzerland, in 1995-1996 and NIMCR-Tsukuba, Japan, in 1996-1998. At LCTS, he is investigating the relationships between synthesis (mainly by CVD), composition, structure and properties of carbon and non-oxide ceramics.

Nathalie Bertrand is an Assistant Professor in the Chemistry Department of the University of Bordeaux since 2003. She completed a Ph.D. in Chemical engineering in 2001 at Toulouse INP. Her main topics of interest concern Gaseous Fluidization, Transport phenomena and Chemical Vapor Deposition. Her current research activities focus on the use of Fluidized Bed-CVD process on short fibers.